Stability and resonant wave interactions of confined two-layer Rayleigh–Bénard systems

S. V. Diwakar, Shaligram Tiwari, Sarit K. Das and T. Sundararajan†

Department of Mechanical Engineering, Indian Institute of Technology Madras, Chennai 600036, India

The current work analyses the onset characteristics of Rayleigh–Bénard convection in confined two-dimensional two-layer systems. Owing to the interfacial interactions and the possibilities of convection onset in the individual layers, the two-layer systems typically exhibit diverse excitation modes. While the attributes of these modes range from the non-oscillatory mechanical/thermal couplings to the oscillatory standing/travelling waves, their regimes of occurrence are determined by the numerous system parameters and property ratios. In this regard, the current work aims at characterising their respective influence via methodical linear and fully nonlinear analyses, carried out on fluid systems that have been selected using the concept of balanced contrasts. Consequently, the occurrence of oscillatory modes is found to be associated with certain favourable fluid combinations and interfacial heights. The further branching of oscillatory modes into standing and travelling waves seems to additionally rely on the aspect ratio of the confined cavity. Specifically, the modulated travelling waves have been observed to occur (amidst standing wave modes) at discrete aspect ratios for which the onset of oscillatory convection happens at unequal fluid heights. This behaviour corresponds to the typical *m:n* resonance where the critical wavenumbers of convection onset in the layers are dissimilar. Based on all of these observations, an attempt has been made in the present work to identify the oscillatory excitation modes with a reduced number of non-dimensional parameters.

Key words: Bénard convection, buoyancy-driven instability, convection in cavities

1. Introduction

A comprehensive characterisation of Rayleigh–Bénard–Marangoni (R–B–M) convection in multiple fluid layers is essential for the understanding of various systems such as Earth mantle convection (Richter & Johnson 1974; Busse 1981) and liquid encapsulated crystal growth (Johnson 1975; Shen *et al.* 1990). The underlying mechanisms of convection in the R–B–M systems can generally be attributed to the isolated/coupled action of buoyancy and capillary forces. The influence of these forces, in conjunction with the thermal and viscous interactions at the fluid–fluid interfaces result in a plethora of unique thermoconvective modes. Notably, parameters such as layer height ratios, container aspect ratios, various property ratios of the fluids and surface tension gradient diversely alter the onset of convection in the layers.

† Email address for correspondence: tsundar@iitm.ac.in

As a result, the multilayer R–B–M flows occasionally exhibit exclusive features such as oscillatory flow excitation and onset of convection even for stable density stratification.

The simplest of multilayer R–B–M systems involves two superimposed layers of immiscible fluids which are subjected to a temperature gradient opposing the direction of gravity (Zeren & Reynolds 1972). Interestingly, such a two-layer system possesses a variety of convection modes even in the absence of interfacial thermocapillary effect. Here, at both the extremes of layer depth ratio (approaching zero or infinity), buoyancy-driven convection is stimulated in the thicker fluid layer due to the effect of unstable density stratification. As a consequence, a weak convection is induced in the other layer through continuity of shear stress at the interface; these modes are labelled (Johnson & Narayanan 1997) as 'lower' or 'upper' dragging modes based on the layer which undergoes primary excitation. However, in the intermediate range of interface heights (determined by property ratios of the fluids), both the fluid layers will be susceptible to undergo simultaneous transition. In these situations, two modes of interactions, namely 'mechanical coupling' (MC) and 'thermal coupling' (TC), can occur between the layers (Rasenat, Busse & Rehberg 1989). The MC mode is characterised by counter-rotating rolls which are formed due to the synchronisation of self-excited convection phenomena in the top and bottom layers. In contrast, the TC mode possesses co-rotating rolls which are separated by a buffer layer that satisfies mechanical continuity at the interface. At certain ranges of depth ratios in between the values corresponding to MC and TC modes (in other words, when the Rayleigh numbers (Ra) in the two layers are equal), competition arises between these states and, eventually, the system may tend to oscillate between them.

The occurrence of oscillatory modes in buoyancy-driven two-layer systems is realisable since the resultant matrix of its linearised system can become non-self-adjoint (Renardy 1996). Correspondingly, the leading eigenvalue of the matrix becomes complex and represents the onset of oscillatory convection. Nevertheless, in order to obtain such non-self-adjoint systems, it is essential for the fluids to have favourable combination of properties (Renardy 1996). To be precise, the property ratio combination $\rho\beta\alpha$ (ρ, density ratio; β, ratio of thermal expansion coefficients; α, thermal diffusivity ratio) should be either much greater or much smaller than unity. Degen, Colovas & Andereck (1998) had accordingly observed the onset of oscillatory convection in silicone oil–water system which has property ratios satisfying the above condition. However, in this case, Nepomnyashchy & Simanovskii (2004) and Simanovskii & Nepomnyashchy (2006) have shown that in addition to the favourable property combination, the presence of thermocapillarity at the interface also plays a decisive role in stimulating oscillations. It is thus evident that the precise parametric conditions for the onset of oscillatory convection in pure buoyancy-driven systems are still not fully identified.

Moreover, the typical manifestation of oscillations in two layer systems occurs via standing wave (SW) or travelling wave (TW) patterns based on the geometric configuration. While the oscillations in infinite (or sufficiently wider) systems happen as TWs, SW phenomena are observed (Colinet & Legros 1994) in smaller-aspect-ratio boxes. Modulated TWs are generally anticipated in the systems with moderate aspect ratios. Here, again, the exact conditions that lead to their occurrence are not precisely known. Yet, the existence of remarkably distinct features at certain aspect ratios of the confined two-layer systems has been widely established. For instance, Johnson & Narayanan (1996, 1997) have observed a dynamic transformation of flow structure in the silicone oil–air system at conditions (aspect ratio) closer to the codimension-two point.

Understandably, the exact parametric conditions for oscillations and associated modulated TWs are buried within the wide ranges of non-dimensional parameters that control the multilayer fluid systems. Thus, the main objective of the current work is to unravel these conditions by performing linear and fully nonlinear analyses on different fluid systems which have been obtained using the 'balanced contrasts' of properties (Colinet & Legros 1994). Owing to this concept, the property ratios of these systems have been balanced in such a way that each of them identically satisfy the criterion proposed by Renardy (1996) (i.e. $\rho\beta\alpha \gg 1$ or $\rho\beta\alpha \ll 1$) and, yet, correspond to a unique value of the parameter a^* (critical height ratio at which Ra values in the two layers are equal). As a consequence of this exercise, it is intended to relate a^* with the occurrence of oscillatory excitation in the two-layer systems and, hence, plausibly reduce the number of non-dimensional parameters that may be required to specify their regimes.

For each of the fluid systems considered in the current work, spectral collocation-based linear stability analysis is first carried out to obtain the critical Ra values for excitation at different depth ratios and cavity aspect ratios. In the process, the linear analysis is also utilised in demarcating the oscillatory and non-oscillatory regimes, thereby facilitating their linkage with the a^* values. Full nonlinear simulations involving the spectral domain decomposition approach are then selectively performed to bring out the resonant wave interactions in the layers. This paves the way for understanding the segregation of oscillatory regimes in confined systems into SW and TW (modulated) modes. Through all of the above means, the current work brings out the physically rich characteristics of confined two-layer systems which have a direct relevance in the liquid encapsulated crystal growth process. Before venturing into further details, a succinct description of the mathematical model and the numerical approach involved in the current analysis is presented in the following section.

2. Mathematical formulation

2.1. *Governing equations and boundary conditions*

Consider two superimposed layers of immiscible fluids which are confined in a two-dimensional cavity of width 'B' and total height '$a_1 + a_2$' (figure 1). The equations governing the buoyancy-driven convection in these fluid layers are given as follows:

(i) **Top layer**

$$\left.\begin{aligned} (\nabla \cdot V_1) &= 0 \\ \frac{1}{Pr_1}\left[\left(\frac{\partial V_1}{\partial t}\right) + (V_1 \cdot \nabla) V_1\right] &= -\nabla p_1 + \nabla^2 V_1 + Ra_1\theta_1\hat{j} \\ \left(\frac{\partial\theta_1}{\partial t}\right) + (V_1 \cdot \nabla)\theta_1 &= \nabla^2\theta_1 \end{aligned}\right\}. \tag{2.1}$$

(ii) **Bottom layer**

$$\left.\begin{aligned} (\nabla \cdot V_2) &= 0 \\ \frac{1}{Pr_1}\left[\left(\frac{\partial V_2}{\partial t}\right) + (V_2 \cdot \nabla) V_2\right] &= -\rho\nabla p_2 + \frac{1}{\nu}\nabla^2 V_2 + \frac{Ra_1}{\beta}\theta_2\hat{j} \\ \left(\frac{\partial\theta_2}{\partial t}\right) + (V_2 \cdot \nabla)\theta_2 &= \frac{1}{\alpha}\nabla^2\theta_2 \end{aligned}\right\}. \tag{2.2}$$
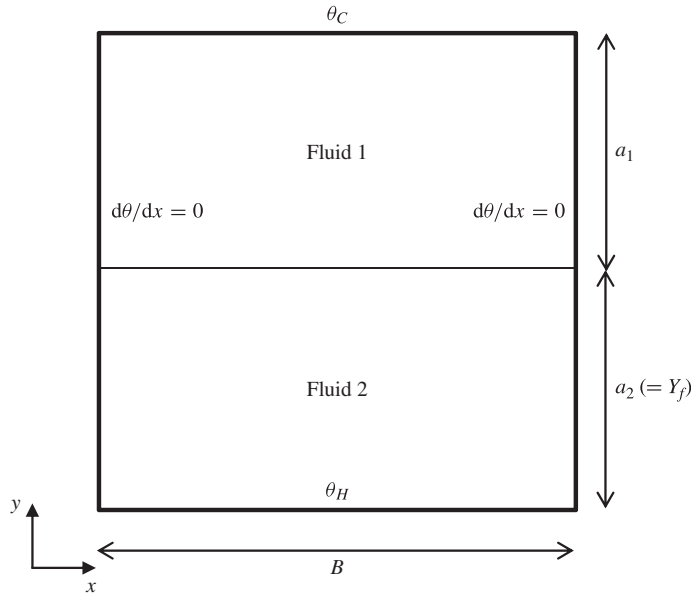
FIGURE 1. Confined two-layer system.

The non-dimensionalisation of the above equations has been achieved using the following scales that pertain to the top layer.

$$L_{ref} = a_1; \quad t_{ref} = a_1^2/\alpha_1; \quad v_{ref} = \alpha_1/a_1; \quad p_{ref} = \rho_1\alpha_1\nu_1/a_1^2. \qquad (2.3a\text{--}d)$$

The symbols ρ, μ, ν, β, α and κ correspond to the ratios between densities (ρ_1/ρ_2), dynamic viscosities (μ_1/μ_2), kinematic viscosities (ν_1/ν_2), thermal expansion coefficients (β_1/β_2), thermal diffusivities (α_1/α_2) and thermal conductivities (κ_1/κ_2) of the top (1) and bottom (2) fluids, respectively. Pr_1 $(= \nu_1/\alpha_1)$ and Ra_1 $(= g\beta_1\Delta\theta a_1^3/\nu_1\alpha_1)$ refer to the Prandtl and Rayleigh numbers of the top layer.

The rigid plates at the bottom and top are maintained at the temperatures of θ_H (hot) and θ_C (cold), respectively. At the same time, the side walls are considered to be rigid and adiabatic. In order to simplify the current analysis, fluid systems involved here are considered to possess large disparity in their densities (conceivably, the bottom layer is heavier). By virtue of this assumption, the interfacial deformation can be neglected in the present configuration since its effect would be commensurate with the other factors which are omitted by means of Boussinesq approximation (Colinet, Legros & Velarde 2001). Hence, at the interface, the non-dimensional flow, momentum and heat transmission conditions are given as follows.

(*a*) Continuity of horizontal velocity: $u_1 = u_2$.
(*b*) Non-deformability of the interface: $v_1 = v_2 = 0$.
(*c*) Continuity of temperature: $\theta_1 = \theta_2$.
(*d*) Continuity of heat flux: $\kappa \partial\theta_1/\partial y = \partial\theta_2/\partial y$.
(*e*) Continuity of tangential stress: $\partial u_1/\partial y - (1/\mu)(\partial u_2/\partial y) = Ma(\partial\theta/\partial x)$.

Here, Ma $(= \sigma_T\Delta\theta a_1/\mu_1\alpha_1)$ corresponds to the Marangoni number at the fluid interface. In order to retain the primary focus on pure buoyancy-driven

convection, *Ma* is set to zero for all of the fluid systems considered in the current analysis.

2.2. *Balanced contrast of property ratios*

From the above mathematical formulation, it is evident that the characteristics of confined two-layer systems are dependent on a large number of distinctive non-dimensional parameters. As a result, their complete estimation becomes tedious as it requires a thorough assessment of the effects manifested by each of the parameters. However, such a comprehensive analysis would be of less importance for the lower/upper dragging modes since their behaviour is essentially governed by the layer which undergoes excitation first. It may be noted that the characteristics of these dragging modes can even be obtained from an equivalent single-layer system whose boundary conditions emulate the other layer's influence. In contrast, the coupled regimes and the oscillatory regimes do not offer a similar convenience and, hence, efforts are now oriented towards the formation of a few non-dimensional groups that can facilitate their characterisation.

As mentioned earlier, the non-dimensional group of property ratios '$\rho\beta\alpha$' suggested by Renardy (1996) forms the basic parameter that can be associated with the occurrence of oscillations in the two-layer systems. The works of Nepomnyashchy & Simanovskii (2004) and Simanovskii & Nepomnyashchy (2006) however indicate that additional groups/parameters are indeed essential for defining the limits of oscillatory regimes exactly. In this regard, the current work focuses on assessing the candidature of the parameter a^* (critical height ratio), which is defined as the layer height ratio (a_2/a_1) at which the Rayleigh numbers of the two layers $(Ra_1 = Ra_2)$ are equal, i.e.

$$a^* = \left(\frac{\beta}{\kappa\alpha\nu} \right)^{1/4}. \tag{2.4}$$

The choice of using a^* for this purpose stems from the convenience it offers in connecting the property ratios of fluid systems with the oscillatory convection phenomena. As is evident from the above relationship (2.4), the parameter a^* depends only on the thermophysical properties and lumps four out of the six non-dimensional ratios $(\rho, \beta, \alpha, \kappa, \nu, Pr_1)$ that are required to characterise pure buoyancy-driven convection in a two-layer system. At the same time, a^* also corresponds to the interfacial height at which the convection phenomena in the two layers exhibit equal propensity and, hence, are capable of yielding oscillatory excitation. But, as observed for silicon oil–water system, not all fluid combinations (despite having a favourable value of $\rho\beta\alpha$) give rise to oscillatory mode of convection and, so, it becomes important to identify their association with the a^* value.

With the above goal, the current work investigates the oscillatory convection characteristics of seven different fluid systems having unique values of a^*. Following the concept of 'balanced contrasts' as suggested by Colinet & Legros (1994), these fluid systems have been obtained by selectively modifying (table 1) certain fluid property ratios to retain the value of $\rho\beta\alpha$. Specifically, property ratios such as $\rho = 0.5$, $\beta = 4$, $\alpha = 2$, $Pr_1 = 1$ are retained the same, so that the resultant fluid combination ($\rho\beta\alpha = 4$) is still favourable to form oscillatory modes (Renardy 1996). The values of a^* have been chosen here in such a way that the resultant critical interfacial heights are obtained as symmetrical pairs with respect to the distance from the cavity half height. Correspondingly, the discussions in the current work will be presented in related pairs of a^* values.

S. no.	a^*	κ	ν	μ
1	0.250	16.00	32.00	16.00
2	0.500	4.00	8.00	4.00
3	0.667	2.25	4.50	2.25
4	1.000	1.00	2.00	1.00
5	1.500	0.4444	0.8889	0.4444
6	2.000	0.25	0.50	0.25
7	4.000	0.0625	0.125	0.0625

TABLE 1. Balanced contrast of properties used for varying a^*.

2.3. Numerical methodology

The characterisation of confined R–B convection in the above fluid systems requires both linear and fully nonlinear approaches for achieving specific objectives. While the linear stability analysis is utilised here for obtaining the critical Rayleigh numbers (Ra_{cr}) and the parametric space for oscillatory excitations, their finer classifications are revealed using the nonlinear approach. In order to be very precise in their respective estimations, these tasks have been accomplished through the spectral collocation method. Specifically, the nonlinear approach has been realised using the domain decomposition method (DDM) that employs an influence matrix (IM) technique for the coupled evolution of flow in the two layers. The salient aspects of these numerical procedures are now briefly discussed in the following subsections.

2.3.1. Linear stability analysis

The present linear approach follows the conventional procedure of linearising the governing equations and boundary conditions over the conductive base state ($V_m = 0$, $\partial\theta_m/\partial x = 0$, $\partial\theta_m/\partial y = \Lambda_m$, where Λ_m is the vertical temperature gradient in each fluid layer m) corresponding to static fluid layers. Taking the confined two-dimensionality of the current configuration into account, the perturbations in the field variables are expanded in terms of normal modes as $\{V'_m, p'_m, \theta'_m\} = \{\widehat{V}_m(x, y), \widehat{p}_m(x, y), \widehat{\theta}_m(x, y)\}e^{\sigma t}$. Resultantly, the semi-discrete equations for the evolution of perturbations are given as follows:

$$\left.\begin{aligned} \nabla \cdot \widehat{V}_m &= 0 \\ \sigma\widehat{V}_m &= -A_m\nabla p_m + B_m\nabla^2\widehat{V}_m + C_m Ra_1\widehat{\theta}_m\widehat{j} \\ \sigma\widehat{\theta}_m &= D_m\nabla^2\widehat{\theta}_m - \Lambda_m\widehat{v}_m \end{aligned}\right\} \qquad (2.5)$$

where $A_1 = B_1 = C_1 = Pr_1$, $D_1 = 1$, $A_2 = \rho Pr_1$, $B_2 = Pr_1/\nu$, $C_2 = Pr_1/\beta$ and $D_2 = 1/\alpha$. The corresponding interfacial conditions are

$$\widehat{u}_1 = \widehat{u}_2, \quad \widehat{v}_1 = \widehat{v}_2 = 0, \quad \widehat{\theta}_1 = \widehat{\theta}_2, \quad \kappa\frac{\partial\widehat{\theta}_1}{\partial y} = \frac{\partial\widehat{\theta}_2}{\partial y}, \quad \frac{\partial\widehat{u}_1}{\partial y} = \frac{1}{\mu}\frac{\partial\widehat{u}_2}{\partial y} \qquad (2.6a\text{–}e)$$

and the boundary conditions are

$$\widehat{V}_m = 0, \quad \widehat{\theta}_m = 0 \text{ (horizontal walls)}, \quad \frac{d\widehat{\theta}_m}{dx} = 0 \text{ (vertical walls)}. \qquad (2.7a,b)$$

Keeping in mind the stringent accuracy requirements for stability solvers, the spatial discretisation of variables in the above formulation has been dealt using spectral collocation scheme. Correspondingly, any variable ϕ (except for pressure which requires a distinct representation) is expanded as a Lagrangian interpolation of the nodal values as

$$\phi_{M,N}(x, y) = \sum_{i=0}^{M} \sum_{j=0}^{N} g_i(x) \, h_j(y) \, \phi(x_i, y_j) \tag{2.8}$$

where M and N are the number of collocation points along the x and y directions, respectively. The cardinal functions $g_i(x)$ and $h_j(y)$ defined over the Gauss–Lobatto–Chebyshev (G–L–C) points, $x_i = \cos(\pi i/M)$ $\{i = 0, 1, \ldots, M\}$ and $y_j = \cos(\pi j/N)$ $\{j = 0, 1, \ldots, N\}$ are specified as

$$g_i(x) = \frac{(-1)^{i+1} \left(1 - x^2\right) T'_M(x)}{\bar{c}_i M^2 (x - x_i)}, \quad i = 0, 1, \ldots, M \tag{2.9}$$

$$h_j(y) = \frac{(-1)^{j+1} \left(1 - y^2\right) T'_N(y)}{\bar{c}_j N^2 \left(y - y_j\right)}, \quad j = 0, 1, \ldots, N. \tag{2.10}$$

Here, $T'_M(x)$ and $T'_N(y)$ correspond to the first derivative of the Mth and Nth Chebyshev polynomial of the first kind. The values of the constants c_i and c_j are 1 for all i and j except at the extremities ($i = 0$ and M or $j = 0$ and N) where they are of value 2. Consequently, any spatial derivative of ϕ at the G–L–C points is obtained by differentiating (2.8) with the additional consideration of discrete orthogonality, i.e. $g_i(x_j) = \delta_{ij}$ and $h_i(y_j) = \delta_{ij}$. The spatial discretisation of the pressure terms requires a special treatment, as it leads to the generation of spurious pressure modes otherwise. Correspondingly, the present work uses the $P_N - P_{N-2}$ approximation where the pressure is approximated through polynomials (given below) of degree $(M - 2, N - 2)$ when the velocity and other variables are represented by polynomials of degree (M, N):

$$p_{M-2,N-2}(x, y) = \sum_{i=1}^{M-1} \sum_{j=1}^{N-1} \hat{g}_i(x) \, \hat{h}_j(y) \, p(x_i, y_j). \tag{2.11}$$

Here, $\hat{g}_i(x)$ and $\hat{h}_j(y)$ are defined as follows:

$$\hat{g}_i(x) = \frac{\left(1 - x_i^2\right)}{\left(1 - x^2\right)} g_i(x) \quad \text{and} \quad \hat{h}_j(y) = \frac{\left(1 - y_j^2\right)}{\left(1 - y^2\right)} h_j(y). \tag{2.12a,b}$$

Using the above polynomial expansions, the system of equations given in (2.5) can be reduced to a generalised eigenvalue problem of the form, $AX = \sigma BX$. This matrix system can then be factorised to yield the spectra of eigenvalues corresponding to any given Ra. Resultantly, Ra_{cr} is obtained by searching for the Ra value at which the real part of the largest eigenvalue (σ_{max}) is zero. In the process, the regimes of oscillatory convection are also identified over the parametric space for which the imaginary part of this largest eigenvalue is non-zero.

The validity of the above linear stability approach is evident from figure 2, where the neutral curves obtained from the current formulation are in close agreement with the published results of Nepomnyashchy & Simanovskii (2004). At this stage, it is to be noted that the curves presented in figure 2 specifically correspond to an unconfined
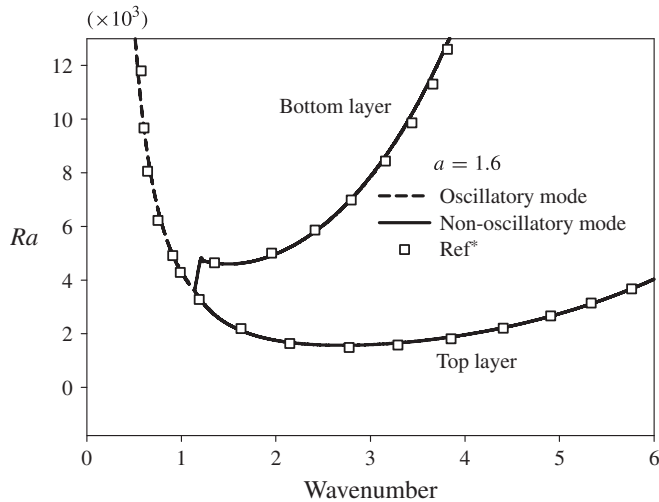
FIGURE 2. Neutral curve for Rayleigh–Bénard convection in infinite two layers of silicone oil and water with $a = 1.6$; Ref* from Nepomnyashchy & Simanovskii (2004).

system of silicone oil and water, with a height ratio of 1.6. Such a utilisation of results from the unconfined systems is presently necessitated by the scarcity of published literature on confined two-layer systems. However, with this confirmation, the validity of the confined formulation can be easily verified by unfolding the unconfined results to yield different neutral curves of confined two-layer systems with free shear walls.

2.3.2. *Spectral domain decomposition approach*

Subsequent to the linear analysis, the task of identifying SW/TW modes within the oscillatory regime is achieved here through nonlinear evaluation of the convection onset characteristics. Considering the fact that these simulations have to be carried out at conditions very close to criticality, usage of highly accurate techniques becomes mandatory. Hence, akin to the linear formulation, the spatial discretisation of flow variables has been performed using spectral collocation which offers 'exponential' or 'infinite order' convergence of errors. However, the restrictions posed by various interfacial discontinuities obviate the use of uniform expansions (Hewitt & Hewitt 1979; Gottlieb & Shu 1997) for the whole domain. This issue is remedied in the current work by employing a spectral DDM where the two fluid domains are distinctly identified and their interface acts as the common boundary. Accordingly, the (mechanically and thermally) coupled evolution of flows in the two domains is evaluated using the IM technique of Dennis & Quartapelle (1983).

The overall procedure of the DDM essentially involves decomposition of the coupled problem into homogeneous and non-homogeneous parts. By virtue of this splitting process, the non-homogeneous set of equations for the two domains are favourably decoupled and are solved using the projection technique (Chorin 1968). On the other hand, the homogeneous equations of the domains are still coupled and require the prediction of interfacial velocity/temperature as a primary task. Hence, the homogeneous solutions are represented here as a superposition of solutions corresponding to various fundamental interfacial modes (Sabbah & Pasquetti 1998). The scalar multipliers associated with the superposition procedure are then obtained

through enforcement of various transmission conditions for the velocity/temperature fields at the interface. This procedure typically leads to the formulation of an IM whose solution at every time step (along with those of the non-homogeneous part) facilitates the transient evolution of flow variables in the two-layer system. The detailed procedures involved in the current implementation and their systematic validation can be accessed from the earlier work of the present authors (Diwakar, Das & Sundararajan 2014).

3. Results

3.1. *Critical behaviour of a fluid system with $a^* = 1.0$*

Using the linear and nonlinear approaches described above, the characterisation of pure Rayleigh–Bénard convection in confined two-layer systems is initiated here by considering a sample fluid system with $a^* = 1.0$ from table 1. Correspondingly, its excitation behaviour is comprehensively studied for different interfacial heights (Y_f) and cavity aspect ratios ($AR = B/(a_1 + a_2)$).

Beginning with a linear stability analysis of the system, the neutral curves for various excitation modes in a cavity of unit height and $AR = 0.5$ are shown in figure 3(*a*). Here, the branches 'Top_1' and 'Bot_1' correspond to the fundamental mode of excitation in the top and bottom fluid layers, respectively. Likewise, branches 'Top_2' and 'Bot_2' represent the next higher mode of excitation in the respective layers. Branch 'Osc' depicts the part of neutral curve for which there is simultaneous onset of oscillatory convection in both the layers. Since the current interest is oriented only towards the prediction of onset behaviour, the focus here is limited to branch 'Osc' and the lowermost parts of the branches 'Top_1' and 'Bot_1'. Correspondingly, figure 3(*b*) and its magnified view in figure 3(*c*) show the least stable part of these curves for different values of *AR* varying from 1.0 to 4.0. In each of these cases, the cubic dependence of *Ra* on the fluid layer thickness (a_1) induces an early onset of convection in the top layer when Y_f is lower than 0.47. This results in the phenomenon of 'upper dragging mode' wherein the bottom layer is passively driven by the continuity of shear stress at the fluid interface. In contrast, an exactly opposite mechanism is observed in the top layer (lower dragging mode) when the interfacial height is more than 0.53, even though the related Ra_{cr} values are the same. It is important to note here that the quasi-symmetric (symmetric except for switching in the least stable mode) behaviour of non-oscillatory neutral curves over $Y_f = 0.5$ is mainly due to the deliberate choice of fluid properties which facilitate such a tendency. However, it will be shown later that this symmetric behaviour is only restricted to the neutral curves whereas their corresponding flow patterns are significantly different at onset.

Incidentally, at interface heights closer to cavity half-height ($Y_f = 0.5$), the branches 'Top_1' and 'Bot_1' cross each other and their interaction leads to the formation of an oscillatory regime (depicted as branch 'Osc'). Here, the propensity for self-excitation in the individual layers becomes nearly the same and the difference in the corresponding Ra_{cr} values becomes marginal. At the beginning ($Y_f \approx 0.48$) and end ($Y_f \approx 0.52$) of this oscillatory range, the system is characterised to be in MC and TC modes (Nataf, Moreno & Cardin 1988) respectively where strong buoyancy-driven convective flows in the two layers interact to form counter-rotating and co-rotating rolls on either side of the interface. In between the cases corresponding to MC and TC modes, both of these states may be cyclically favoured and this results in the generation of oscillatory convection patterns within the domain.
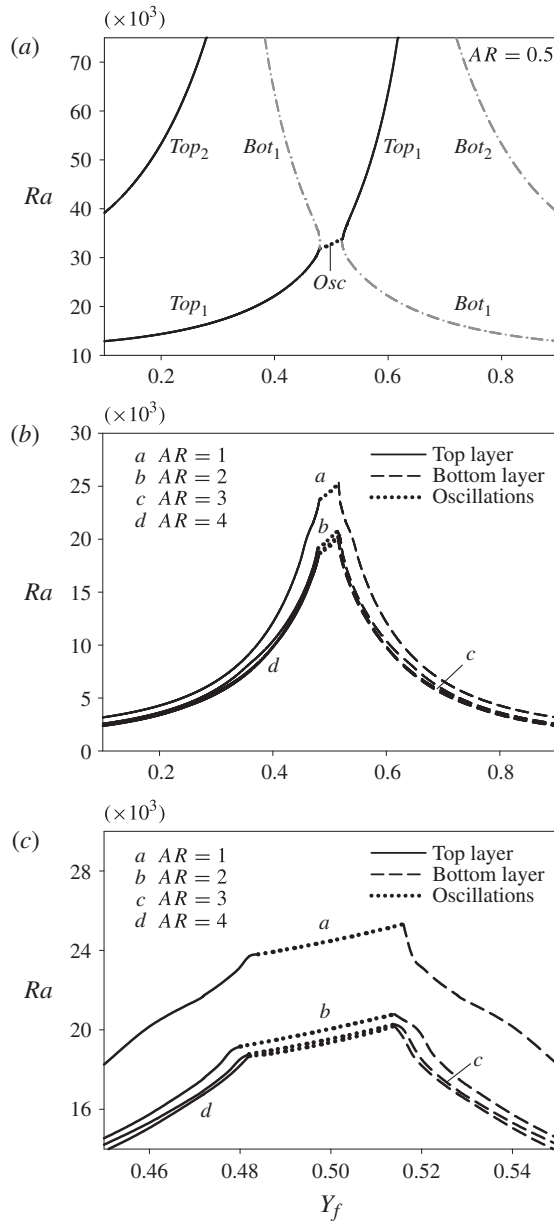
FIGURE 3. Neutral curves at different aspect ratios: (*a*) $AR = 0.5$; (*b*) other higher *AR*; (*c*) magnified view of (*b*).

More information on the above oscillatory and non-oscillatory modes can also be perceived by varying *AR* of the system at fixed values of Y_f. These are now explained in the following subsections with the help of full nonlinear simulations.

3.1.1. *Non-oscillatory modes* $(0 < Y_f \leqslant 0.48; 0.52 \leqslant Y_f < 1.0)$

Focusing attention on the non-oscillatory flow regimes first, a two-layer system of unit height and $Y_f = 0.40$ is now chosen to illustrate the flow features of confined
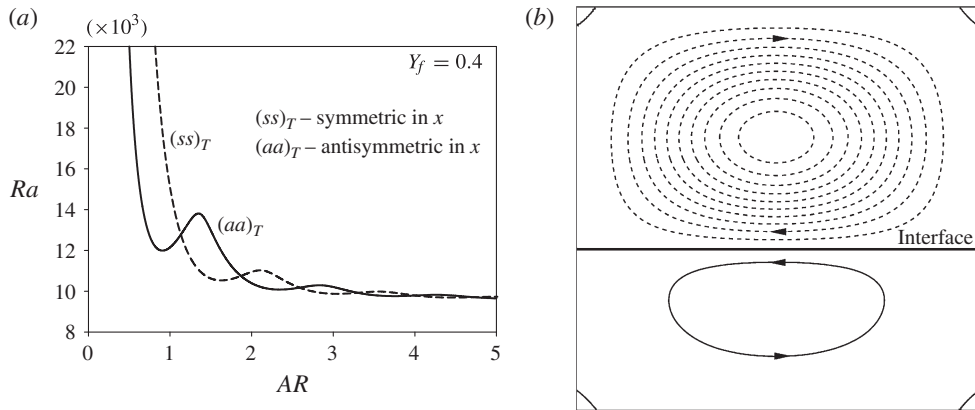
FIGURE 4. Onset characteristics of the confined two-layer system with $a^* = 1.0$ and $Y_f = 0.40$: (*a*) neutral curves; (*b*) streamlines of flow at $AR = 1.0$.

upper dragging mode. The corresponding neutral curves are shown in figure 4(*a*). For the sake of clarity, only the neutral curves which at some point may become the least-stable mode are shown here. In the present case, they correspond to the top layer since it attains early criticality at lower Y_f values. It may be noted that it is possible to associate the attributes of these curves with an equivalent confined single-layer system whose bottom wall mimics the effects manifested by the bottom layer. This can be ascertained from the fact that frequent mode switching (from $(ss)_T$ to $(aa)_T$ and vice versa as shown in figure 4*a*) manifested at discrete values of *AR* are governed by the aspect ratio of the top layer and not by the cavity aspect ratio. The symmetric (or the asymmetric) nature of the modes are defined here with respect to the cavity mid-plane in the *x* direction. Figure 4(*b*) shows the streamlines of flow evaluated through nonlinear simulations at $AR = 1.0$ and Rayleigh number slightly higher ($\epsilon = (Ra - Ra_{cr})/Ra_{cr} = 0.002$) than the corresponding critical value (Ra_{cr}). The convention adopted here to represent the streamlines facilitate an easier qualitative comparison of flow in the layers. Accordingly, the number of streamlines in each layer acts as an indicator of the relative strength of convection in that layer. At the same time, the sense of rotation of the rolls is indicated by differentiating the streamlines via continuous solid and dashed lines. While the positive stream-function contours (anticlockwise rolls) are represented by solid lines, the negative stream-function contours (clockwise rolls) are represented through dashed lines. In order to clearly demarcate the zones of various convection rolls, iso-stream-function contours of zero value (even though this might not perfectly qualify as a streamline) have also been included in all of the streamline plots. Correspondingly, all the contour lines that have any end point on the rigid wall boundary correspond to this zero stream-function contour. From figure 4(*b*), the features of upper dragging mode are clearly evident as strong buoyancy driven clockwise convection in the top layer induces a weak anti-clockwise circulation in the bottom layer. The diagonal lines as observed in the four corners represent the zero stream-function contours that demarcate the corner vortices from the main convection rolls.

In contrast to the above behaviour, distinctive features are observed at a higher interfacial position ($Y_f = 0.48$). From the corresponding neutral curves shown in figure 5(*a*), the presence of intermittent oscillatory regimes can be observed in certain
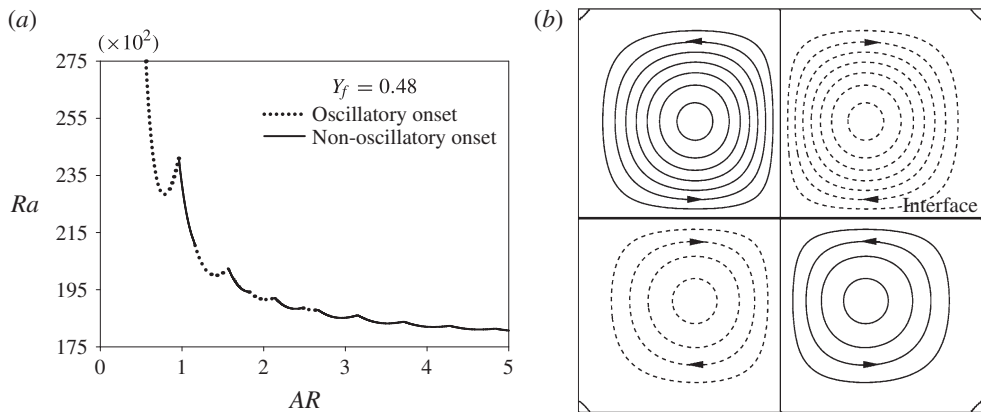
FIGURE 5. Onset characteristics of the confined two layer system with $a^* = 1.0$ and $Y_f = 0.48$. (a) Neutral curves; (b) streamlines of flow at $AR = 1.0$.

lower ranges of AR values due to the pronounced effect of lateral confinement. Here, the solid parts of the neutral curves correspond to the excitation curves of the top layer, whereas the dotted parts represent the merged excitation curves of both the top and bottom layers and indicate the onset of oscillatory convection. Adhering to the present focus on non-oscillatory modes, flow simulations have been performed just above criticality for a confined system of $AR = 1$. The resultant streamline patterns are shown in figure 5(b), where evidently the strength of convection in each of the layers reveals their tendency for self-excitation. However, the slight dominance of convection in the top layer aided by lower thermal expansion coefficient and kinematic viscosity of the bottom layer coerces excitation in the bottom layer to mechanically synchronise with that of the top layer (MC). Correspondingly, the interface between the two layers is rendered as an isotherm. Since the increase of interfacial height (from 0.40 to 0.48) increases the local aspect ratio of top layer, flow excitation occurs here at a higher mode number and, hence, a dual loop structure is observed.

Interestingly, the situation at the interfacial height of $Y_f = 0.52$ is completely contrary to the above scenario. The regimes for the onset of oscillatory convection here have narrowed down to a large extent (figure 6a). Also, the solid parts of neutral curves now correspond to the least-stable modes in the bottom layer as the interfacial height of $Y_f = 0.52$ favours an early onset of convection in that layer. Furthermore, a remarkable change can be seen in the streamline plots of figure 6(b) where the two layers are subjected to convection rolls of same orientation. This result can be explained as follows. By virtue of its larger thickness, the bottom layer is subjected to intense convection which results in non-uniform heating of the interface. Specifically, for the dual loop structure formed at $AR = 1$, the mid-portion of the interface becomes hot. Such a temperature distribution coupled with the higher thermal expansion coefficient in the top layer causes fluid particles to rise in that layer. The larger magnitude of buoyancy force available in the top layer thus overwhelms the dragging effect created at the interface by the bottom layer convection and eventually, macro co-rotating rolls (with respect to the convection loops in the bottom layer) are formed in the top layer also. In the process, mechanical continuity at the interface is satisfied through the creation of a small buffer layer in the interfacial zone where weak rolls counter-rotate with respect to the macro rolls of both the layers. As a consequence, a large amount of dissipation happens in this buffer zone.
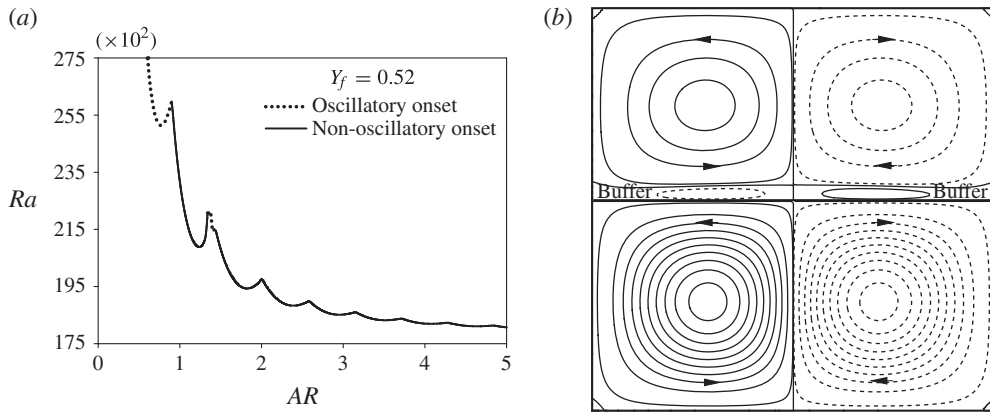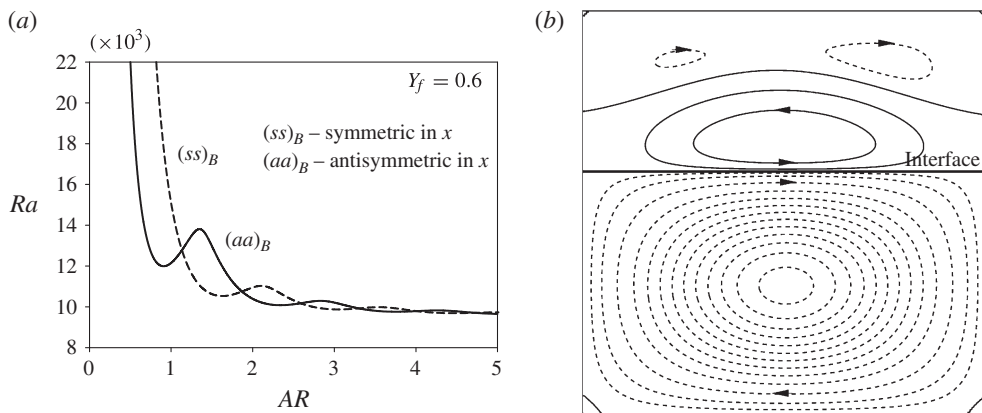
(a)

(b)

FIGURE 6. Onset characteristics of the confined two-layer system with $a^* = 1.0$ and $Y_f = 0.52$: (a) neutral curves; (b) streamlines of flow at $AR = 1.0$.

(a)

(b)

FIGURE 7. Onset characteristics of the confined two-layer system with $a^* = 1.0$ and $Y_f = 0.60$; (a) neutral curves; (b) streamlines of flow at $AR = 1.0$.

On increasing the interfacial height further to $Y_f = 0.60$, it can be observed that the resultant neutral curves (figure 7a) are identical to the case of $Y_f = 0.40$ (figure 4a), except for the present association of least stable modes with the bottom layer. However, such an apparent quasi-symmetric transition about the cavity half-height is restricted only to the neutral curves. The resultant flow patterns shown in figure 7(b) are visibly different from the situation at $Y_f = 0.40$. Here, the streamline patterns clearly reveal the dominance of convection in the bottom layer and the enlargement of counter-rotating convection roll (driven by viscous dragging at the interface) which marginalises the co-rotating vortex zone of the top layer. With any additional increase in the interfacial height, it can be expected that the co-rotating roll weakens and the counter-rotating convection zone completely encompasses the top layer. Interestingly, in figure 7(b), an asymmetry can be observed in the two co-rotating rolls at the top. This is mainly caused due to a peculiar interaction between the TC and MC processes. It can be recalled that at $Y_f = 0.52$ (figure 6b), the top layer consisted of a dual loop convection roll which had the same rotational orientation as that of the

bottom layer. However, with the increase of interfacial height to $Y_f = 0.60$, the strong buoyancy-driven convection in the bottom layer transitions from a dual loop structure to a single loop structure. At the same time, the counter-rotating roll in the top layer (which was originally a small buffer zone) also becomes single looped and possesses a contrasting influence on the weak co-rotating rolls at the top. In other words, the counter-rotating roll aides the clockwise rotating roll on the top right while it opposes the anticlockwise rotating roll on the top left. Owing to its strength, it is even able to coerce a change in the rotational orientation of weak co-rotating roll on the top left. As a result, an asymmetric (with respect to the vertical mid-plane) configuration of flow is observed for this interfacial height. With the further increase in interfacial height, the self-excitation tendency of the top layer reduces and the system can be expected to regain its antisymmetric feature.

Figure 8 shows the streamlines for the above non-oscillatory modes at a slightly higher AR of 3. Here, the previously discussed flow behaviour of different modes are essentially retained except for the increase in number of rolls and the change in configuration (symmetric or asymmetric) which are determined by the corresponding least-stable modes of excitation. Noticeably, in all of these cases, the convection rolls at the ends are affected by the presence of lateral walls.

3.1.2. *Oscillatory modes* $(0.48 < Y_f < 0.52)$

Following the characterisation of non-oscillatory modes, the mechanisms of oscillatory convection are now analysed in a representative two-fluid system with $Y_f = 0.50$. The respective neutral curves obtained from the linear stability analysis are shown in figure 9. Once again, only the least-stable parts of the neutral curves are utilised here for representing the onset behaviour. Evidently at this cavity half-height, the excitation of oscillatory flow is observed for all of the aspect ratios. Also, the presence of local peaks at discrete aspect ratios indicates mode switching of convection rolls (number and type of symmetry) at those points. In order to understand the corresponding flow pattern, nonlinear simulations are now performed for a particular system with $AR = 3$. Figure 10 shows the temporal sequence of streamlines in half a period of the oscillatory pattern. It can be clearly observed that the rotational orientation of MC rolls are periodically reversed here by the occurrence of ephemeral TC modes. Notably, the change from MC to TC is initiated in the top layer by virtue of its higher thermal expansion coefficient. In other words, the predominance of buoyancy force in the top layer induces a local reversal of flow direction for any small heat perturbation transferred across the interface. Once the strength of convection increases in the top layer, the small buffer layer associated with the TC mode shifts its location from the top layer to bottom fluid layer. This buffer zone then transiently grows in the bottom layer and brings about a new configuration of MC that is exactly opposite to the initial one. Subsequent flow reversal from the MC configuration is once again initiated by the onset of TC characteristics in the top layer and not by backtracking the path that led to the new MC mode. As a result, the system exhibits a hysteretic cycle since the forward and backward paths between the two MC or TC modes are different.

In order to quantify the nature of the wave mechanism in the above oscillatory case, velocity values are temporally monitored at various points in both the layers as shown in figure 11. Figure 12 shows the temporal variation of u-velocity at points B4 and T4 after the flow fields in both the top and bottom layers have transiently converged to a proper periodic state. It is observed that at both of these points, the signature of the velocity signal conforms to a typical sinusoidal function that implies
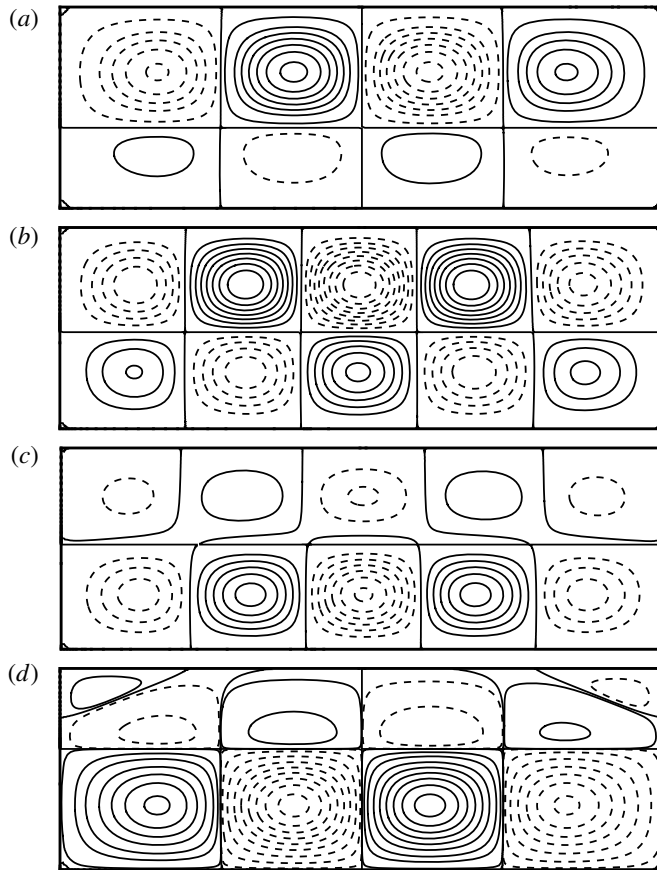
FIGURE 8. Streamlines of flow in the confined two-layer system with $AR = 3.0$ and: (*a*) $Y_f = 0.40$; (*b*) $Y_f = 0.48$; (*c*) $Y_f = 0.52$; (*d*) $Y_f = 0.60$.

a SW phenomenon. Figure 13 shows the phase plots obtained by correlating velocity signals between points B3 and B5 and points B3 and T5. The linear contravariance of v-velocity at points B3 and B5 of the bottom layer (figure 13*a*) clearly represents the formation of a SW with asymmetric rolls along the horizontal direction of the cavity. On the other hand, the elliptical phase variation between points B3 and T5 is due to the sequence of changes in flow patterns as explained in the previous paragraph. For the current two-layer system with the chosen properties and $Y_f = 0.50$, the SW pattern is observed invariably at all of the lower values of aspect ratios considered. However for an unconfined system, Colinet & Legros (1994), Nepomnyashchy & Simanovskii (2004) have shown that TW patterns are normally expected. From the very slight asymmetry of streamlines observed for the current case of $AR = 3$ as opposed to perfect symmetry observed for $AR = 1$ presented in the work of Diwakar *et al.* (2014), it can be speculated that the increase of this asymmetry with increase in AR may lead to a TW at infinite horizontal extent.

The time period for oscillations here is generally determined by the transport and thermophysical properties of both of the fluids since the oscillations are formed due to the competing influence of TC and MC processes. However, for a given
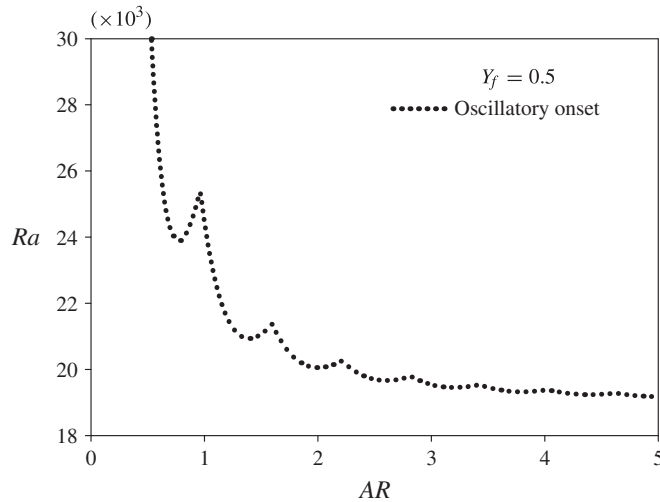
FIGURE 9. Neutral curves for the onset of flow in a confined two-layer system with $a^* = 1.0$ and $Y_f = 0.50$.

fluids combination, the oscillation time period depends on the thermal constraint (Ra) applied to the system. As shown by Colinet & Legros (1994), both the SW and TW mechanisms have a limited range of existence above the threshold. Upon gradually increasing the Ra value from Ra_{cr}, they have observed an increase in harmonics of the temporal transport property variation. Resultantly, the time period of the oscillations increases and beyond a certain value of Ra, the system will end up in a state of steady MC.

3.2. *Oscillatory onset characteristics for the fluids system with $a^* = 0.667$ and 1.50*

Proceeding further with the other fluid systems mentioned in table 1, the onset behaviour is now described for a confined two-layer system of unit height and $a^* = 0.667$ (third row of table 1). The critical interface height (Y_f^*) for equality of Rayleigh numbers in the two layers of the system is 0.4. With respect to this system and the others to follow, efforts will be expended only on understanding their oscillatory regimes since they are the true manifestations of strong two-layer interactions.

Figure 14(a) shows the neutral curves (with respect to interfacial heights) of the above system obtained at different values of AR varying from 1.0 to 4.0. A magnified view of the oscillatory regime in this figure is shown in figure 14(b). It is evident from the latter figure that the change of least-stable mode from top layer to bottom layer occurs here through an oscillatory regime closer to the expected value of Y_f^*. However, in comparison with the scenario at $a^* = 1.0$, there is a reduction in the range of interfacial heights over which the onset behaviour is oscillatory. Interestingly, $AR = 1.0$ is devoid of any oscillatory transition zone and the reason for this could be understood by analysing the variation of onset characteristics with AR at a fixed Y_f closer to Y_f^*. Correspondingly, figure 15(a) and its magnified view in figure 15(b) show the least-stable segments of neutral curves at different aspect ratios and a fixed interfacial height of $Y_f = 0.41$. From the figure, it is evident that the overlapping pattern of various modes has resulted in non-oscillatory onset of flow for a narrow
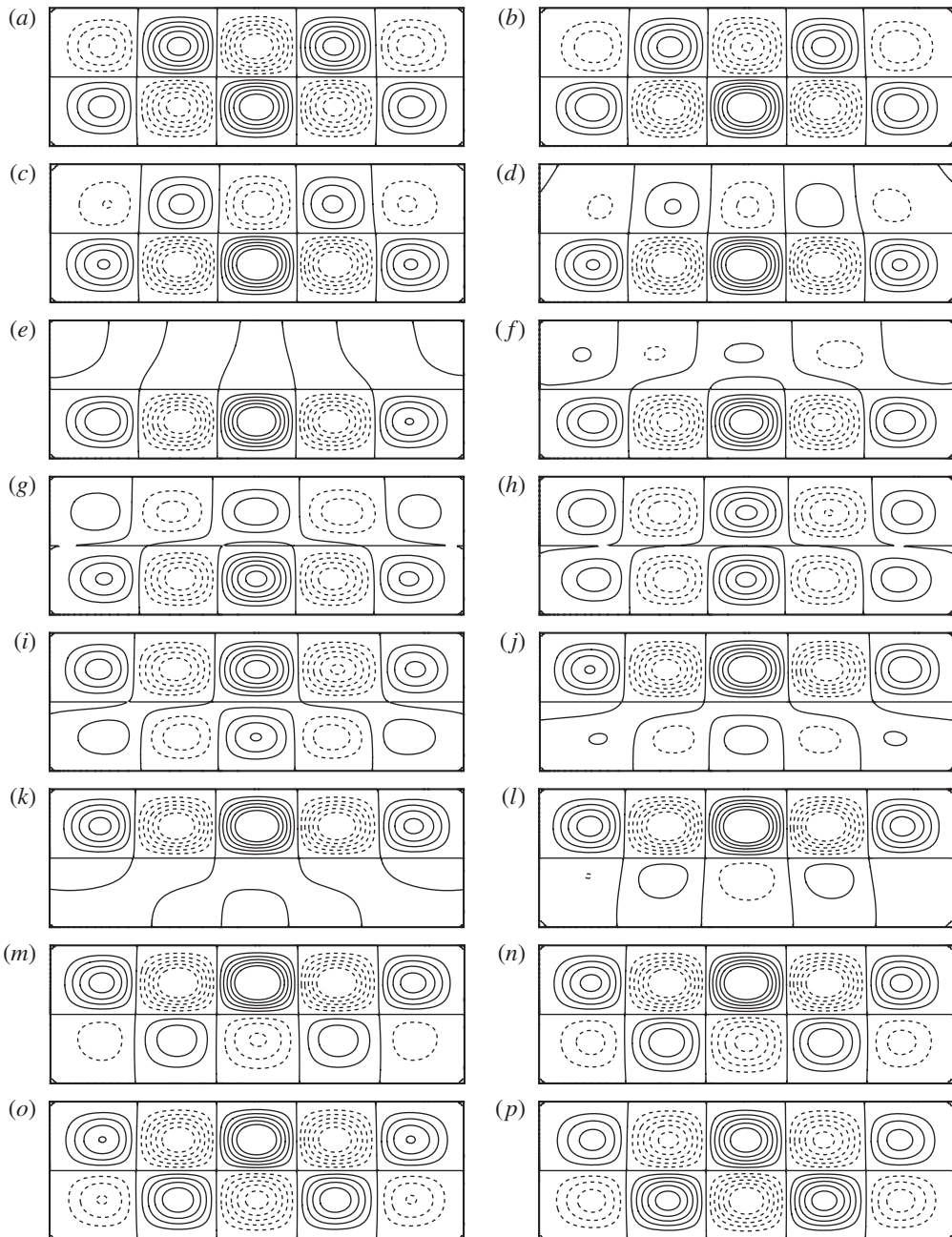
FIGURE 10. Streamlines of flow showing SW mechanism at onset for $AR = 3.0$ and $Y_f = 0.50$: (*a*) $t = 0$; (*b*) $t = T/30$; (*c*) $t = T/15$; (*d*) $t = T/10$; (*e*) $t = 2T/15$; (*f*) $t = T/6$; (*g*) $t = T/5$; (*h*) $t = 7T/30$; (*i*) $t = 4T/15$; (*j*) $t = 3T/10$; (*k*) $t = T/3$; (*l*) $t = 11T/30$; (*m*) $t = 2T/5$; (*n*) $t = 13T/30$; (*o*) $t = 7T/15$; (*p*) $t = T/2$.

regime around $AR = 1.0$. Also, the presence of local peaks at discrete aspect ratios are seen beyond $AR > 1.2$ where mode switching of convection rolls can be expected.

Taking the effects of lateral cavity walls into account, it would be reasonable to expect SW patterns similar to those observed in the previous section for all lower
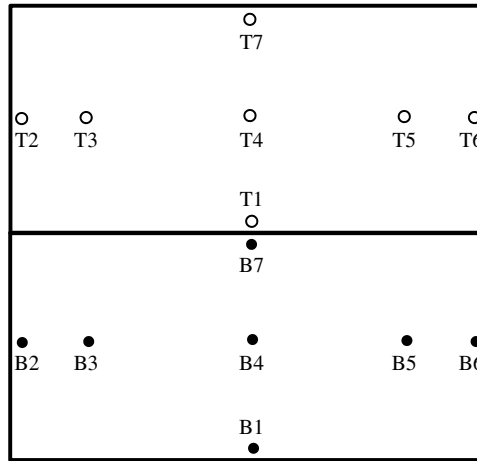
FIGURE 11. Locations of monitoring points for two-layer systems with onset of oscillatory convection.
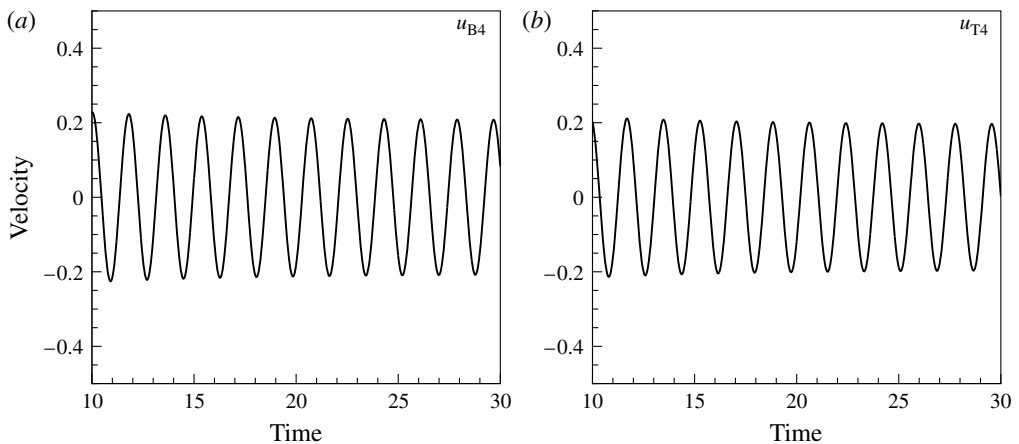
FIGURE 12. Temporal variation of v-velocity at various points: (*a*) B4; (*b*) T4.

values of *AR*. Correspondingly, a SW pattern is observed for a sample system with $AR = 2.35$ and $Y_f = 0.41$. The related temporal evolutions of streamlines for the full period of oscillations are shown in figure 16. As indicated by the vertical arrows at $t = 0$ and $t = T$, the changes with respect to time occur only between the top and bottom layers (SW) with no lateral movement of the circulation patterns. The arrows signify the heat and momentum exchanges in the vertical direction across the interface and not any fluid movement. Following the SW mechanism explained earlier, the system here undergoes perpetual switching between the MC and TC modes with a slight asymmetry observed along the horizontal direction. It can also be observed that the critical wave mode for both the layers is essentially the same and hence, the predominant number of rolls in both the layers is equal to three. Upon increasing the *AR* value to 2.45, the number of rolls in each layer increases to four and this is evident from the corresponding instantaneous streamline plots presented for a full time period in figure 17. Once again, a typical SW behaviour is observed wherein the MC mode
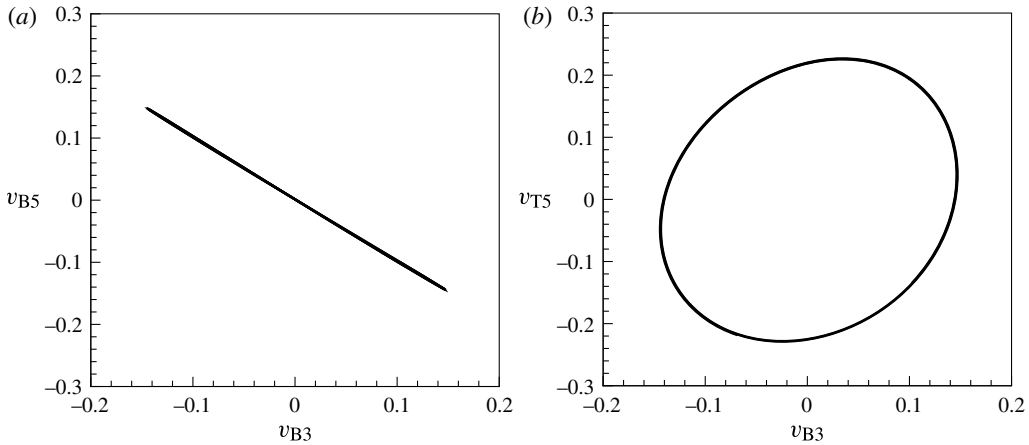
FIGURE 13. Phase variations in v-velocity of different points on the domain: (*a*) B3 versus B5; (*b*) B3 versus T5.
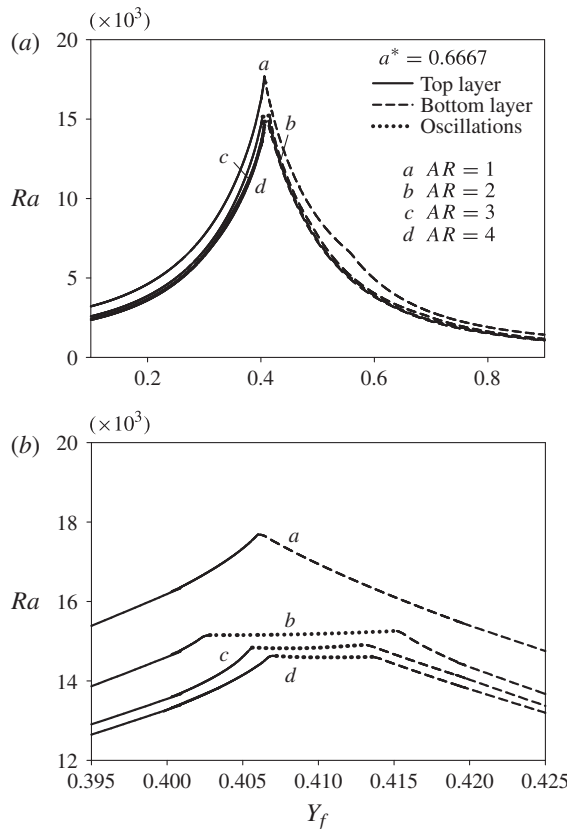
FIGURE 14. (*a*) Neutral curves for the two-layer system with $a^* = 0.667$. (*b*) Magnified view of (*a*).

is periodically reversed by the TC mode which originates in the top layer due to its higher β value. In stark contrast to these features, a peculiar behaviour is observed at a selected aspect ratio closer to the mode switching point (in-between the values
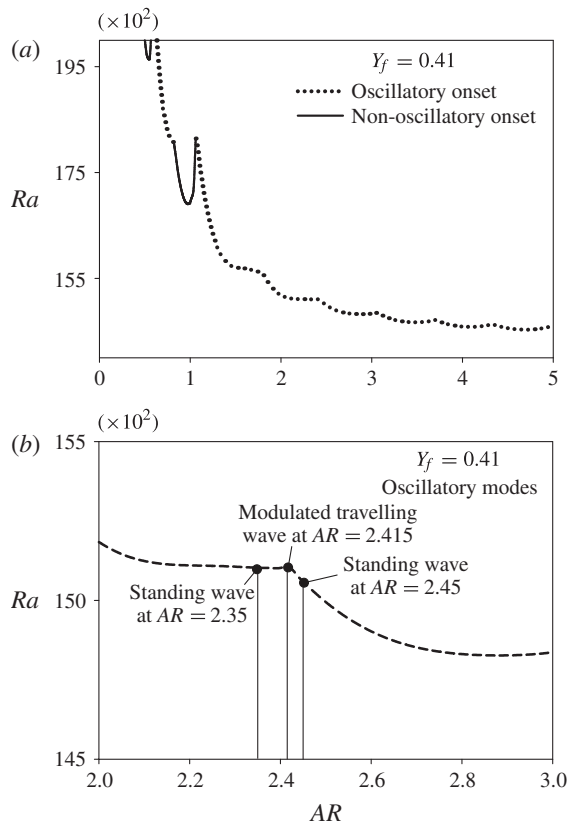
FIGURE 15. (*a*) Neutral curves corresponding to interfacial height $Y_f = 0.41$ for the two-layer system with $a^* = 0.667$. (*b*) Magnified view of (*a*) around $AR = 2.5$.

2.35 and 2.45). Figures 18 and 19 show the temporal evolution (truncated from a full cycle) of streamlines corresponding to the two layer system with $AR = 2.415$. Here, in addition to the local reversal of flow direction (as in a SW), the rolls are subjected to back and forth lateral motion along the horizontal direction, as indicated by the arrows. Such a combination of flow characteristics clearly corresponds to a typical modulated TW, which can be attributed to the mismatch of critical wavenumbers of excitation in the confined two layers. It can be clearly seen that at this value of *AR*, the individual aspect ratios of the top and bottom layers result in their critical excitation at mode numbers three and four, respectively. As a result of this non-similar excitation, there is a dynamic adjustment of rolls in the individual layers and thus a modulated TW pattern is evolved. Such a dynamic response of the system can also be associated with the conventional $l:l + 1$ resonance, where l is the lowest mode number corresponding to the two layers. However, this behaviour is slightly different from that of the Takens–Bogdanov bifurcation (Renardy, Renardy & Fujimura 1999) which deals with the interaction of two real eigenvalues with a complex conjugate pair. In the current case, the point of $l:l + 1$ resonance deals with the interaction of two complex conjugate pairs. It may be noted that modulated TWs were not observed at mode switching points in the case of fluid system with $a^* = 1.0$ since their excitation does not happen as $l:l + 1$ resonance.
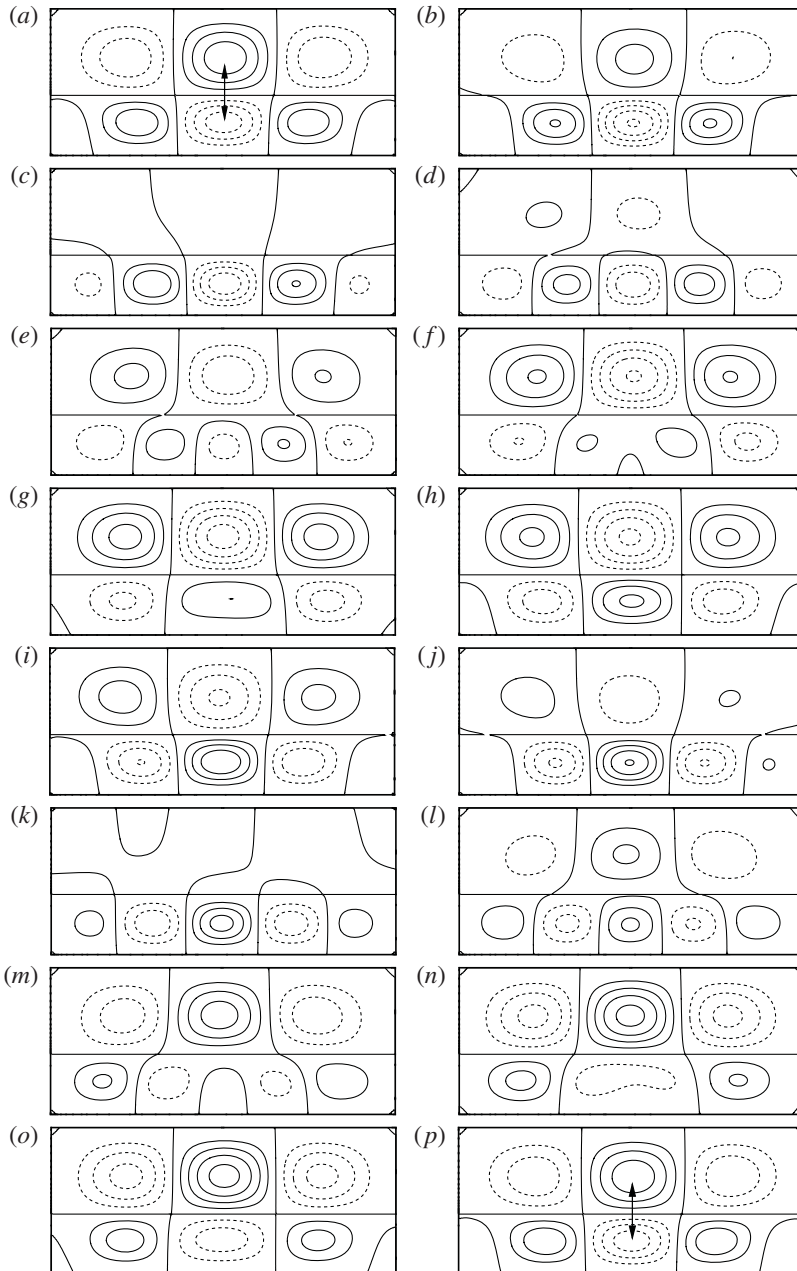
FIGURE 16. Streamlines of flow showing SW mechanism at onset for $a^* = 0.667$, $AR = 2.350$ and $Y_f = 0.41$: (*a*) $t = 0$; (*b*) $t = T/15$; (*c*) $t = 2T/15$; (*d*) $t = T/5$; (*e*) $t = 4T/15$; (*f*) $t = T/3$; (*g*) $t = 2T/5$; (*h*) $t = 7T/15$; (*i*) $t = 8T/15$; (*j*) $t = 3T/5$; (*k*) $t = 2T/3$; (*l*) $t = 11T/15$; (*m*) $t = 4T/5$; (*n*) $t = 13T/15$; (*o*) $t = 14T/15$; (*p*) $t = T$. (A video of the above dynamics is available as online supplementary material available at http://dx.doi.org/10.1017/jfm.2014.359.)
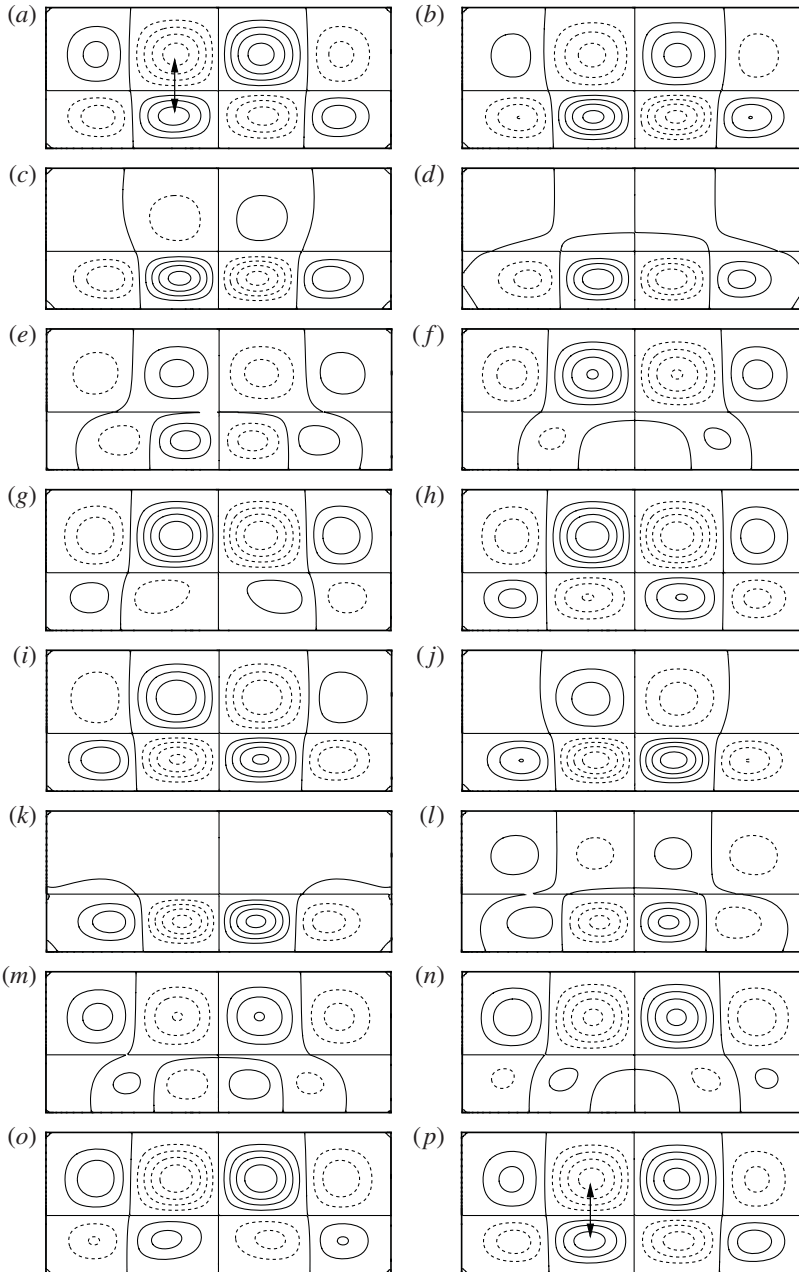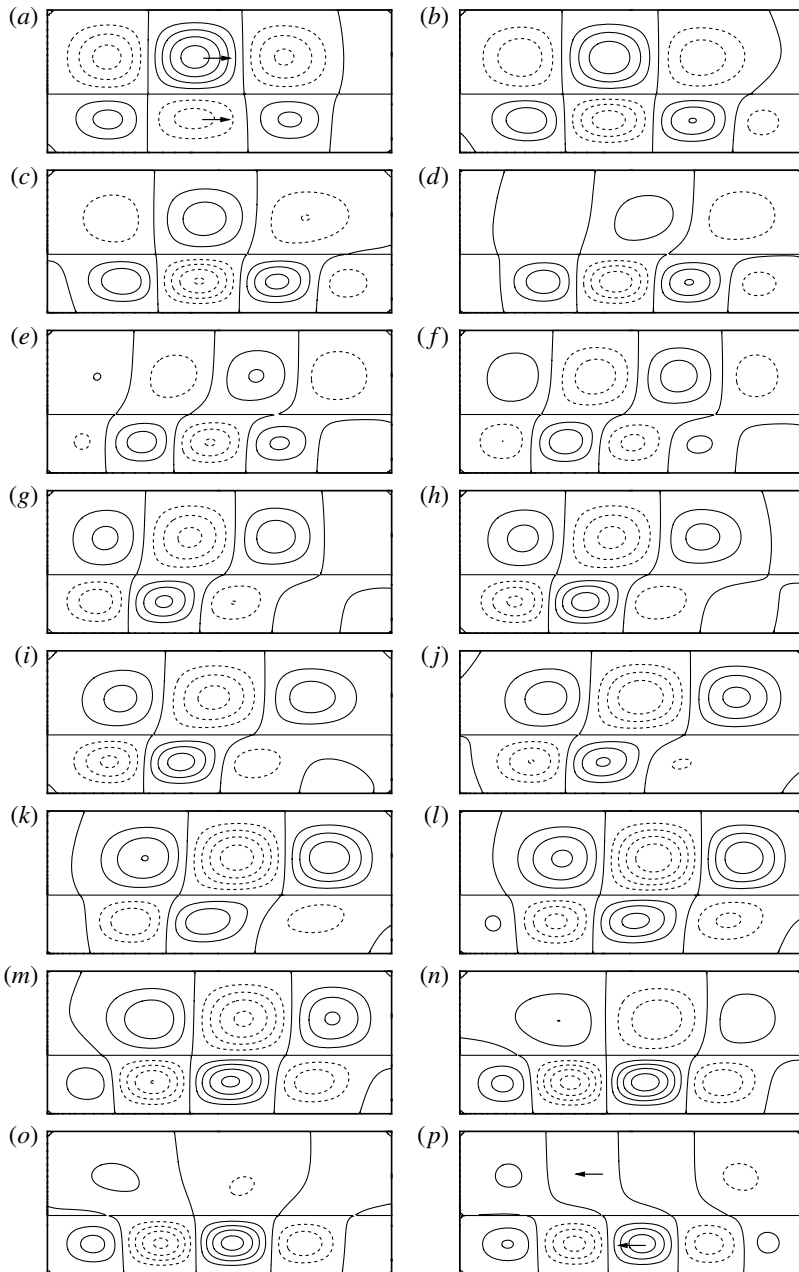
FIGURE 17. Streamlines of flow showing SW mechanism at onset for $a^* = 0.667$, $AR = 2.45$ and $Y_f = 0.41$: (a) $t = 0$; (b) $t = T/15$; (c) $t = 2T/15$; (d) $t = T/5$; (e) $t = 4T/15$; (f) $t = T/3$; (g) $t = 2T/5$; (h) $t = 7T/15$; (i) $t = 8T/15$; (j) $t = 3T/5$; (k) $t = 2T/3$; (l) $t = 11T/15$; (m) $t = 4T/5$; (n) $t = 13T/15$; (o) $t = 14T/15$; (p) $t = T$. (See the online supplementary movie.)

The comparison of temporal variations (figure 20) in v-velocity at points B4 and T4 for the above aspect ratios clearly reveals the amplitude modulation of an otherwise sinusoidal wave at $AR = 2.415$. Noticeably, the time plots reveal that the
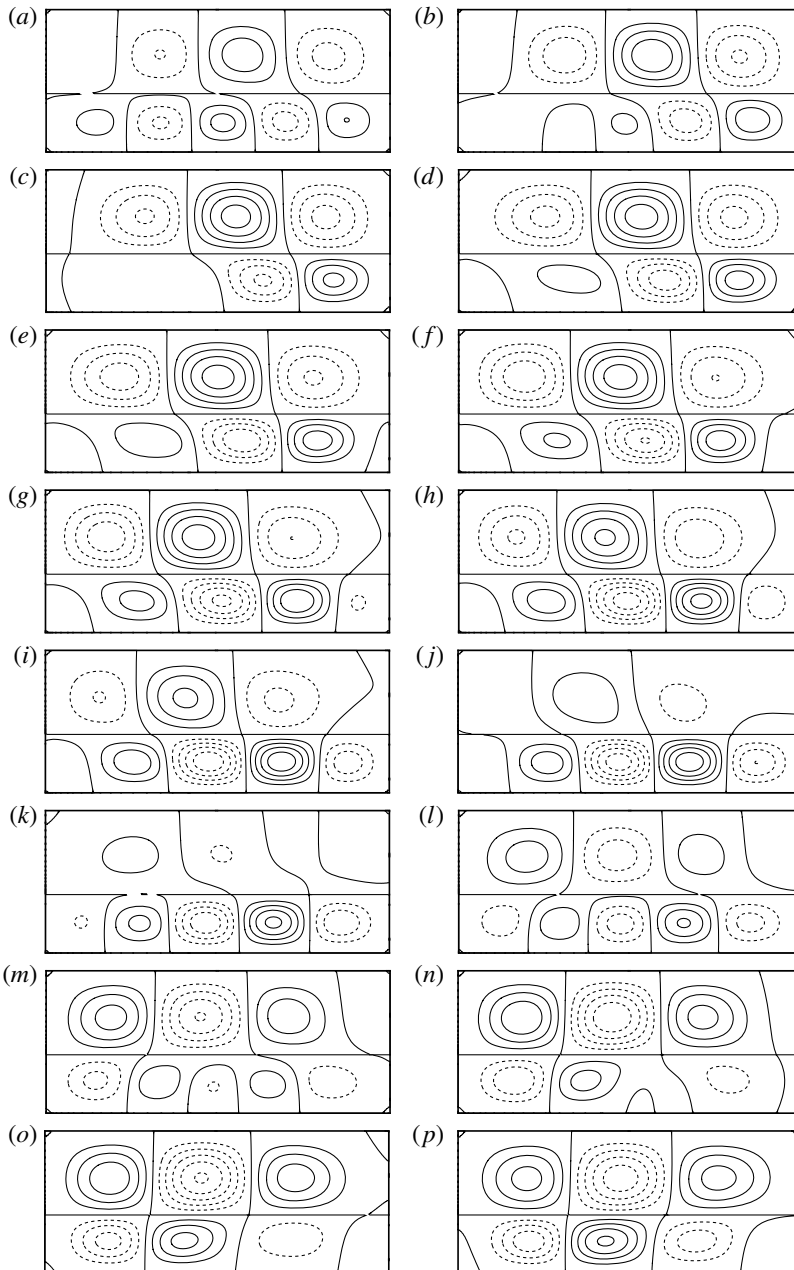
FIGURE 18. Streamlines of flow showing a quasi-periodic modulated TW mechanism at the onset for $a^* = 0.667$, $AR = 2.415$ and $Y_f = 0.41$: (*a*) $t = 291.2$; (*b*) $t = 291.4$; (*c*) $t = 291.6$; (*d*) $t = 291.8$; (*e*) $t = 292.0$; (*f*) $t = 292.2$; (*g*) $t = 292.4$; (*h*) $t = 292.6$; (*i*) $t = 292.8$; (*j*) $t = 293.0$; (*k*) $t = 293.2$; (*l*) $t = 293.4$; (*m*) $t = 293.6$; (*n*) $t = 293.8$; (*o*) $t = 294.0$; (*p*) $t = 294.2$.

TW phenomenon at $AR = 2.415$ is not truly periodic as compared with the SWs observed for $AR = 2.35$ and $AR = 2.45$. This is evident from the tiny shifts in the peaks of modulated wave that can be observed in figure 20(*c*,*d*). The reason for such a

FIGURE 19. Streamlines of flow showing a quasi-periodic modulated TW mechanism at the onset for $a^* = 0.667$, $AR = 2.415$ and $Y_f = 0.41$ (continued): (*a*) $t = 294.4$; (*b*) $t = 294.6$; (*c*) $t = 294.8$; (*d*) $t = 295.0$; (*e*) $t = 295.2$; (*f*) $t = 295.4$; (*g*) $t = 295.6$; (*h*) $t = 295.8$; (*i*) $t = 296.0$; (*j*) $t = 296.2$; (*k*) $t = 296.4$; (*l*) $t = 296.6$; (*m*) $t = 296.8$; (*n*) $t = 297.0$; (*o*) $t = 297.2$; (*p*) $t = 297.4$. (See the online supplementary movie.)

behaviour can be deduced from the corresponding fast Fourier transform (FFT) shown in figure 21 which reveals the presence of some significant subharmonic (figure 21, inset) and superharmonic modes for the quasi-periodic modulated TW. Their effects
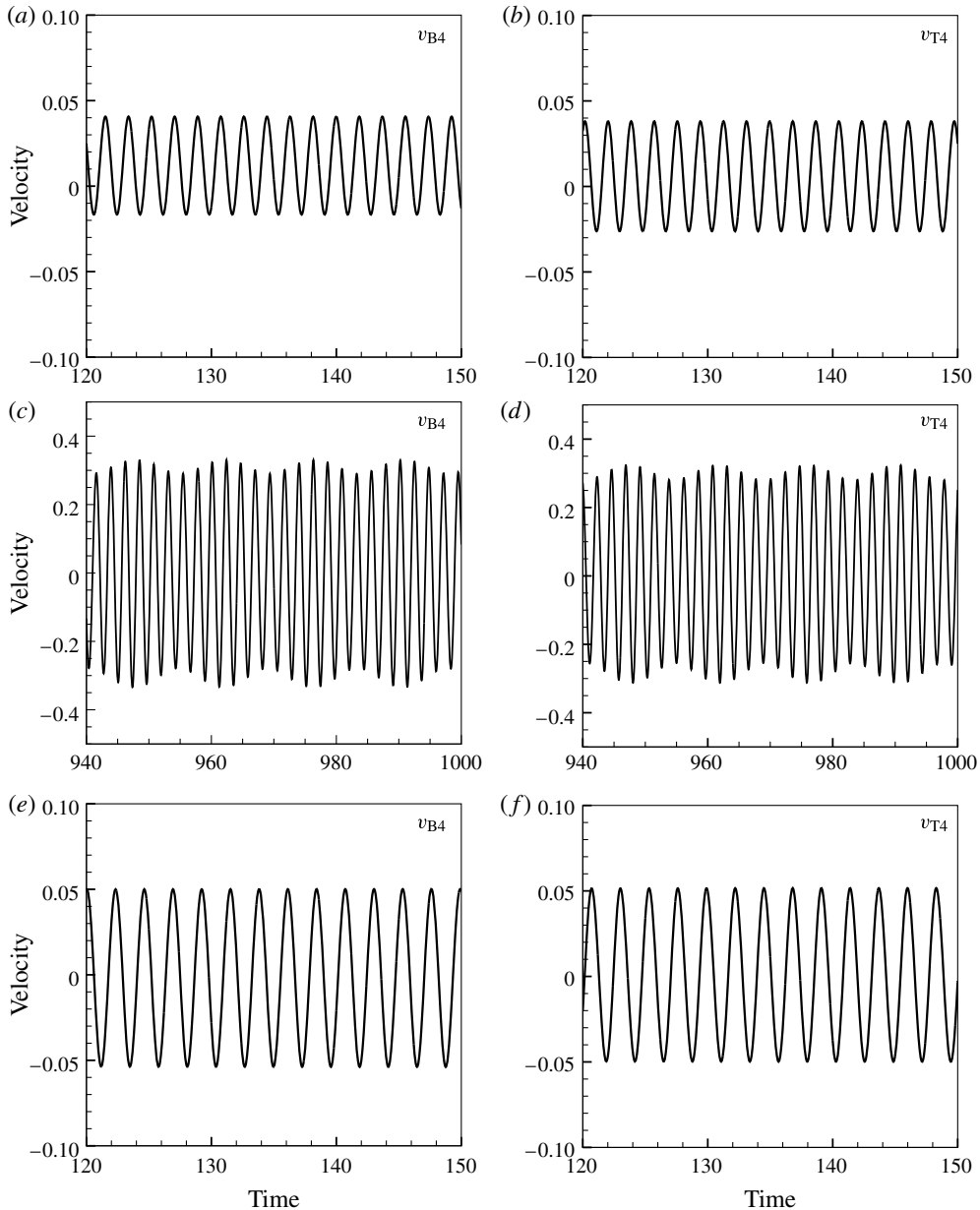
FIGURE 20. Temporal variation of v-velocity at various points on systems with $a^* = 0.667$: (*a*) B4 at $AR = 2.35$; (*b*) T4 at $AR = 2.35$; (*c*) B4 at $AR = 2.415$; (*d*) T4 at $AR = 2.415$; (*e*) B4 at $AR = 2.45$; (*f*) T4 at $AR = 2.45$.

are also visible in the related phase plots of figure 22, which are drawn between v-velocity at different points on the top and bottom layers. The elliptical trajectories of phase plots at $AR = 2.35$ (shown in figure 22*a*,*b*), clearly reveal a contravariance of v-velocity between the chosen points through the alignment of its major axis. The length of minor axis indicates the level of asymmetry present in the fluid layers even
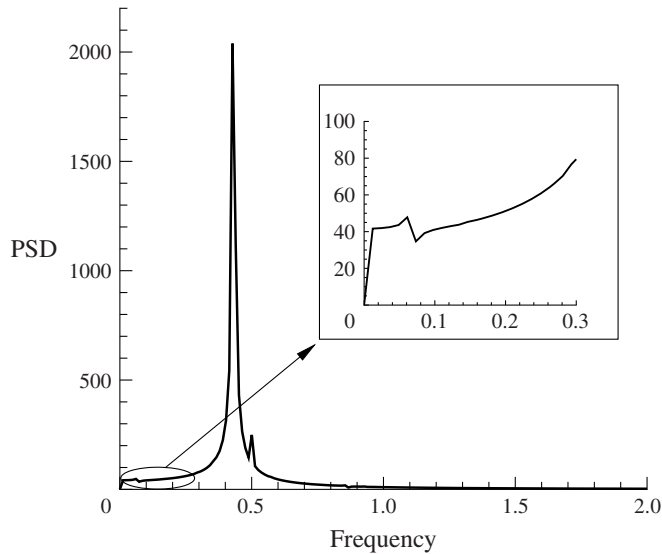
FIGURE 21. FFT of the v-velocity signal corresponding to figure 20(c).

though they are characterised to be associated with a SW. In contrast, the scenario at $AR = 2.45$ is characterised by a direct covariance of v-velocity at corresponding points in the two layers. The absence of any lateral attribute clearly signifies the exact spatial symmetry of flow features in both the layers. By virtue of their complex nature, the phenomena in both the top and bottom layers for $AR = 2.415$ are characterised by a transient and gradual alternation between the covariant and contravariant states. This is clearly evident from the intricate trajectory followed by the phase plots at $AR = 2.415$, even though some orderliness is observed in the time plots shown in figure 20. The subharmonic and superharmonic contributions seen in the spectrum of figure 21 have actually evolved during the later part of simulations over a modulated carrier wave of fixed amplitude and frequency. The future course of evolution for the case with $AR = 2.415$ is unclear and it could get into a chaotic attractor mode or something else entirely different. Only a very long time transient analysis, which is beyond the scope of present work, could lead to a definite conclusion.

The behaviour of two-layer system with $a^* = 1.50$ is quite identical to its counterpart at $a^* = 0.667$ except for the previously described bottom layer phenomena now occurring in the top layer. The corresponding fluid property ratios are given in the fourth row of table 1. The least-stable parts of the neutral curves related to this rigidly confined two-layer system are shown in figure 23(a). Once again, the closeness of oscillatory regime to the expected value of critical interfacial height ($Y_f^* = 0.6$) is evident from the magnified view in figure 23(b). Akin to the case of $a^* = 0.667$, a direct jump of critical characteristics from the top layer to the bottom layer (absence of non-oscillatory regime) is observed at $AR = 1.0$. Figure 24 shows the least-stable parts of the neutral curves at $Y_f = 0.59$ where it can be observed that intermittent non-oscillatory regimes exist at lower values of AR, owing to the overlapping patterns of various fundamental modes. In addition to these non-oscillatory zones, local peaks at distinct aspect ratios can also be observed where modulated TWs will be present in contrast with SW modes at nearby aspect ratios. For the current fluid system, one such occurrence can be identified at $AR = 2.40$ where there is an active interaction
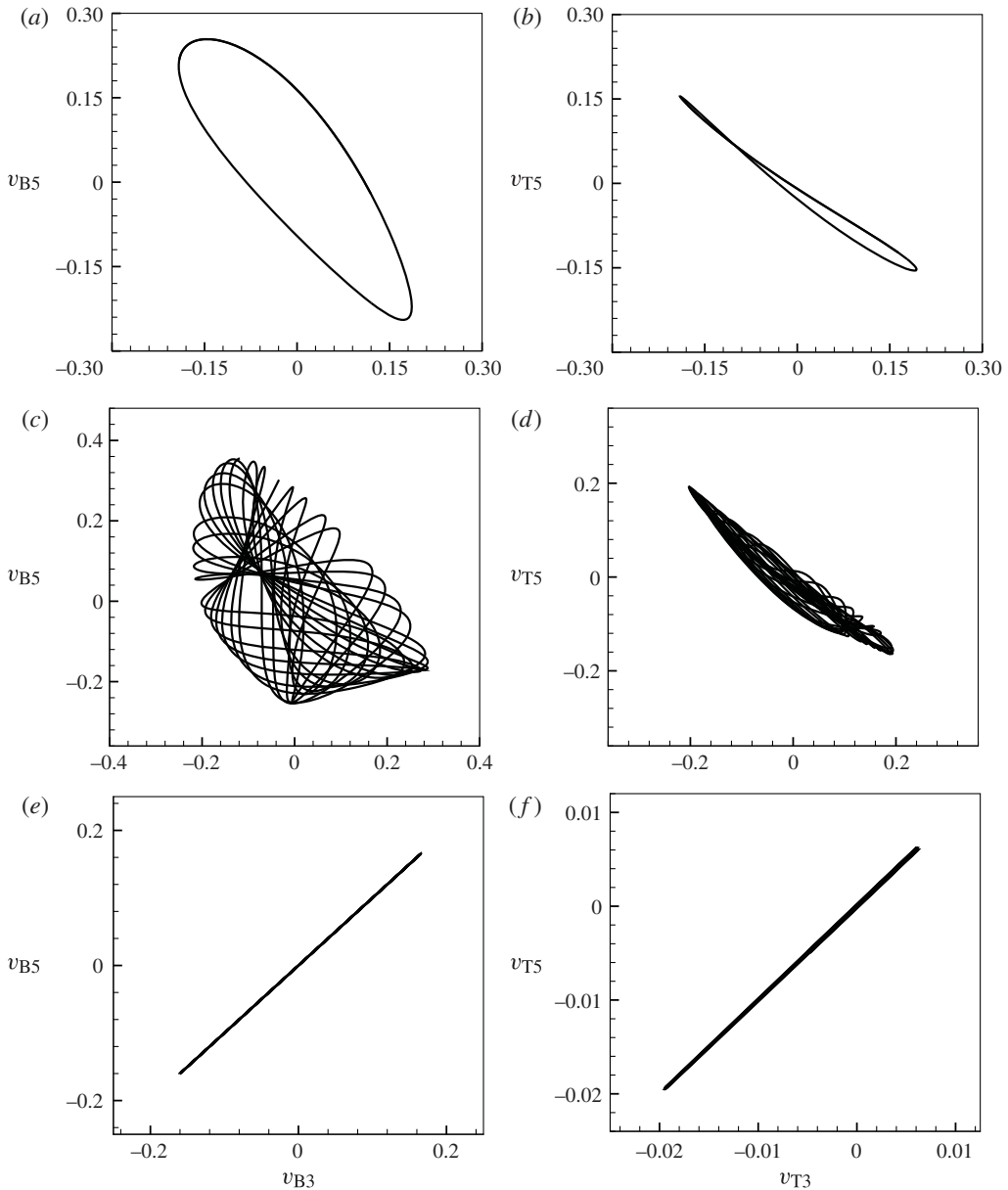
FIGURE 22. Phase variations in v-velocity of different points on the domain for $a^* = 0.667$: (*a*) B3 versus B5 at $AR = 2.35$; (*b*) T3 versus T5 at $AR = 2.35$; (*c*) B3 versus B5 at $AR = 2.415$; (*d*) T3 versus T5 at $AR = 2.415$; (*e*) B3 versus B5 at $AR = 2.45$; (*f*) T3 versus T5 at $AR = 2.45$.

between the fourth mode of top layer and the third mode of bottom layer. For the sake of conciseness, the plots related to the temporal evolution of streamlines are not presented here. Rather, the characteristics of these oscillatory modes are clearly brought out through the time (figure 25) and phase plots (figure 26) corresponding to various points in the top and bottom layers. Identical to the system with $a^* = 0.667$,
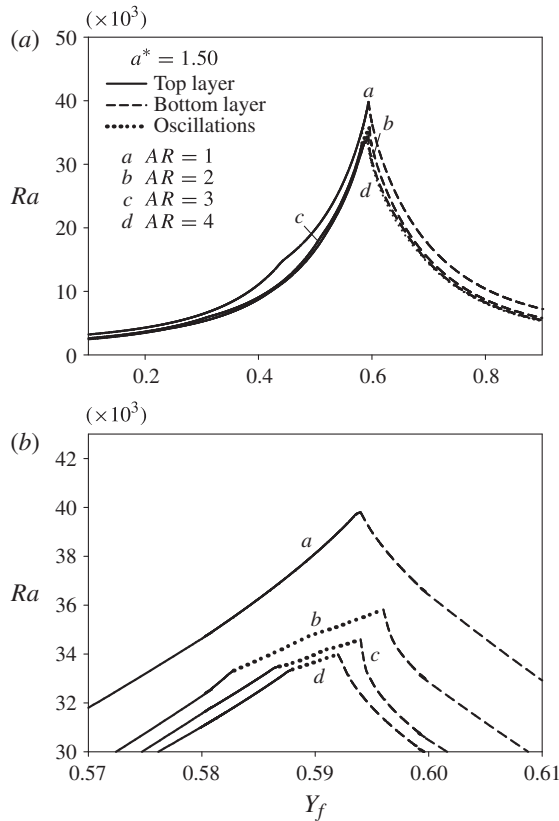
FIGURE 23. (*a*) Neutral curves for the two-layer system with $a^* = 1.50$. (*b*) Magnified view of (*a*).

the occurrence of modulated wave pattern (figure 25*c*,*d*) in between two regular sinusoidal variations can be observed. Similarly, the phase variations of *v*-velocity at points on the top and bottom layers (figure 26) reveal the presence of a single trajectory for the cases with $AR = 2.30$ and $AR = 2.60$. In between these cases, it can be clearly observed that a complex and transient trajectory for the phase plots is followed due to the modulated TW phenomena occurring in the top and bottom layers.

3.3. *Oscillatory onset characteristics for the fluid system with* $a^* = 0.5$ *and* 2.00

In the case of fluid systems with $a^* = 0.5$ and $a^* = 2.0$ from table 1, the critical interfacial position (Y_f^*) moves closer to the top and bottom horizontal walls, respectively. As a consequence, the parametric window for oscillations (with respect to interfacial heights) in these two-layer systems narrows down and is visible only after significant enlargement of the figure as shown in figure 27. This behaviour can be corroborated with figures 28 and 29 where the least-stable parts of the neutral curves obtained at fixed interfacial heights, are presented. In contrast to the behaviour observed for $a^* = 0.667$ or $a^* = 1.5$, the oscillatory zones have shrunk to a few smaller patches at lower values of *AR*. Clearly, this behaviour corresponds to the overlapping pattern of various neutral curves wherein the primary criticality is determined by the non-oscillatory modes at higher *AR* values. In order to understand
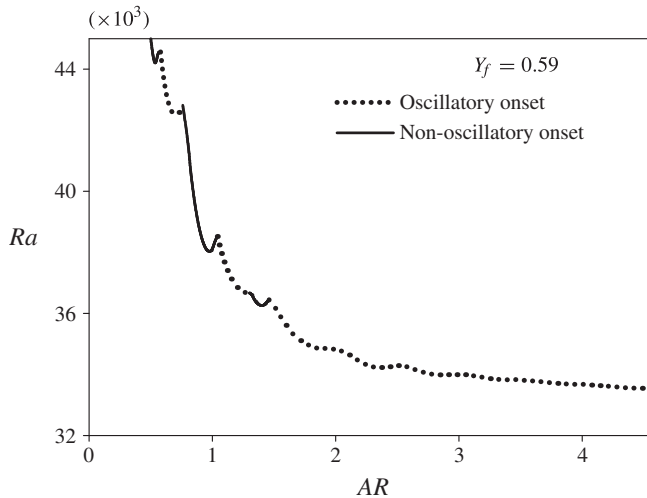
FIGURE 24. Neutral curves corresponding to interfacial height $Y_f = 0.59$ for the two-layer system with $a^* = 1.50$.

the flow features in the smaller window of oscillatory regime, a two-layer system with $a^* = 0.50$, $Y_f = 0.351$ and $AR = 1.0$ is now analysed. Figure 30 shows the instantaneous streamlines obtained for a full period of oscillations in the domain. The system clearly reveals a modulated TW behaviour wherein the rolls in the bottom layer periodically change their rotational orientation and also undergo a back and forth motion along the horizontal direction of the cavity. However, the top layer is characterised by the presence of a SW which is slightly modulated by the TW of the bottom layer. The main reason for such a behaviour can be attributed to the occurrence of critical interfacial heights closer to the extrema (0 or 1). This correspondingly results in a large disparity between the aspect ratios of the top and bottom layers and so, the disparate critical modes in the two layers favour the formation of modulated TWs within the confined system. For the system under consideration, it can be clearly observed that the mode numbers corresponding to the top and bottom layers are one and three, respectively. An exactly reversed behaviour is observed (not shown here) for the system with $a^* = 2.00$, $Y_f = 0.649$ and $AR = 1.0$ where the rolls in the top layer undergo a periodic change in rotational orientation and also back and forth horizontal motion. Despite these manifestations of modulated TWs in the streamline plots, the time plots for the system with $a^* = 0.5$ (and also for $a^* = 2.0$) shown in figure 31 are devoid of any low-frequency amplitude modulation as observed in the cases of $a^* = 0.667$ and $a^* = 1.50$. The reason for this phenomenon could be a perfect match in the frequencies associated with the reversal of roll orientation and the back and forth motion of the rolls. However, the phase variations in the v-velocity (figure 32) at various points in both the layers reveal a typical TW pattern where orientation of the major axis of intersecting loops represent a contravariance between these points on the same layer (associated with odd mode number). The lateral thickness of the phase loops indicate the phase lags brought in due to the presence of TWs.

3.4. *Convection onset characteristics for systems with $a^* = 0.25$ and $a^* = 4.00$*

Finally, for the two-layer systems with $a^* = 0.25$ and $a^* = 4.00$, the critical interface heights are much closer to the top and bottom horizontal walls. This leads to the
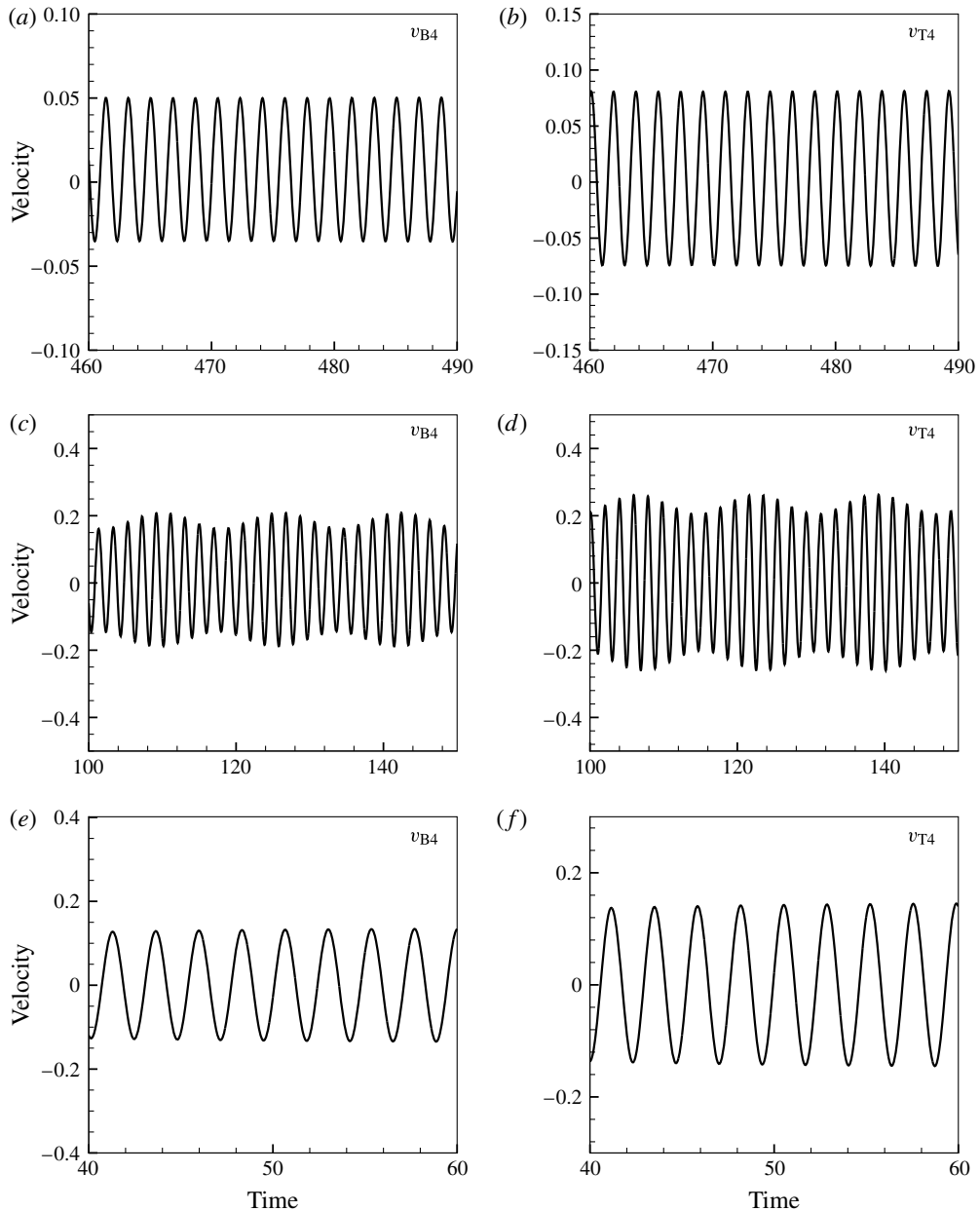
FIGURE 25. Temporal variation of v-velocity at various points on systems with $a^* = 1.50$: (*a*) B4 at $AR = 2.30$; (*b*) T4 at $AR = 2.30$; (*c*) B4 at $AR = 2.40$; (*d*) T4 at $AR = 2.40$; (*e*) B4 at $AR = 2.60$; (*f*) T4 at $AR = 2.60$.

complete disappearance of the intermediate oscillatory zone, as can be seen in figure 33. As a result, there is an abrupt change of criticality from the top layer to the bottom layer as the interfacial height is gradually increased in the two-layer system with the above-mentioned properties. This behaviour can be corroborated from figures 34 and 35 which depict stationary streamline patterns at interfacial heights
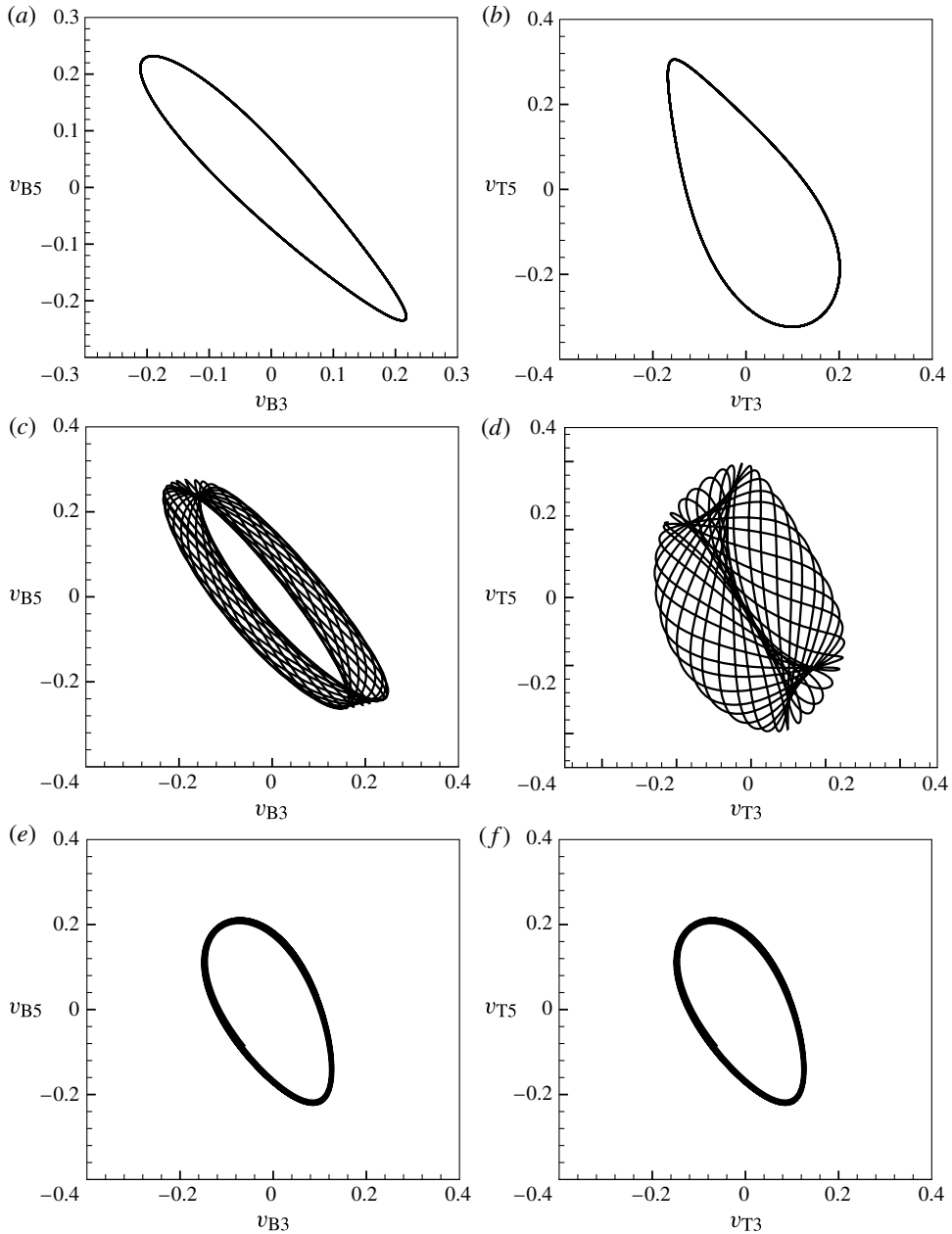
FIGURE 26. Phase variations in v-velocity of different points on the domain for $a^* = 1.50$: (*a*) B3 versus B5 at $AR = 2.30$; (*b*) T3 versus T5 at $AR = 2.30$; (*c*) B3 versus B5 at $AR = 2.40$; (*d*) T3 versus T5 at $AR = 2.40$; (*e*) B3 versus B5 at $AR = 2.60$; (*f*) T3 versus T5 at $AR = 2.60$.

just above and below the critical interfacial height. The strong convection present in the top layer at Y_f very slightly less than Y_f^* abruptly transfers to the bottom layer upon crossing the critical interfacial height and evidently, the fluid combinations are devoid of any oscillatory patterns.
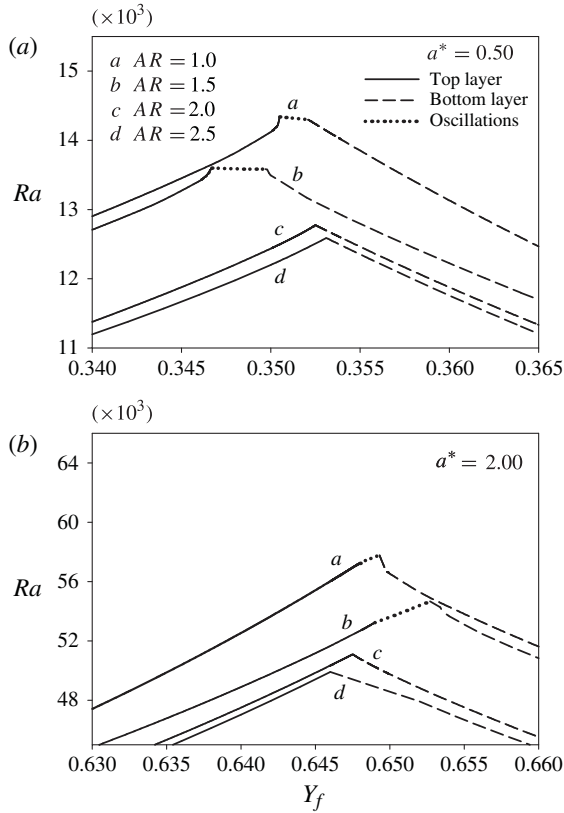
FIGURE 27. Neutral curves for the two-layer system with (*a*) $a^* = 0.50$ and (*b*) $a^* = 2.00$.
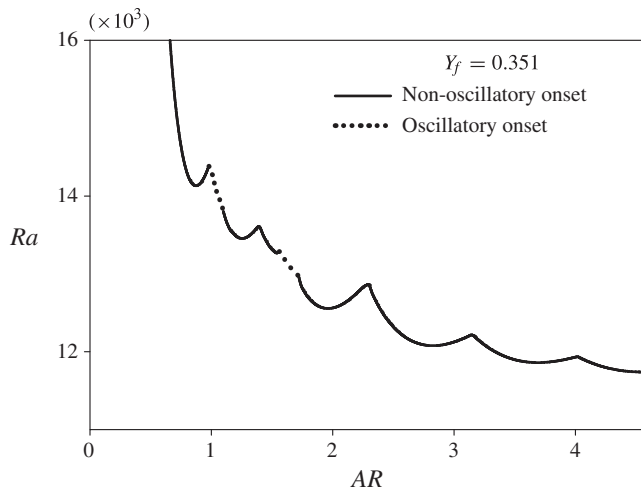

FIGURE 28. Neutral curves corresponding to interfacial height $Y_f = 0.351$ for the two-layer system with $a^* = 0.50$.
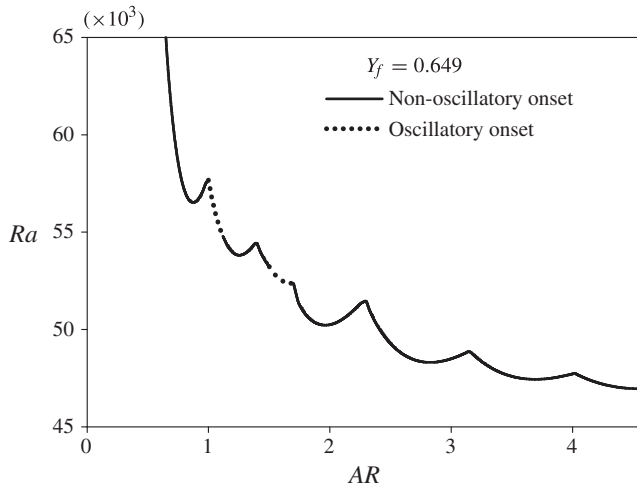
FIGURE 29. Neutral curves corresponding to interfacial height $Y_f = 0.649$ for the two-layer system with $a^* = 2.00$.

3.5. *Remarks*

Before summarising the outcomes of the above balanced contrast analysis, it becomes essential to examine some of its aspects more closely. Primary among them concerns the uniqueness and the exclusivity of the obtained results to $\rho\beta\alpha$ and a^* values considered in table 1. In other words, it is important to understand the behaviour of fluids that have alternative combinations of properties and, yet, yield the same values of $\rho\beta\alpha$ and a^*. For this purpose, a linear stability analysis is now carried out on fluid systems that have been obtained through the balanced contrasts of properties corresponding to silicone oil–water combination. These new fluids (listed in the first three rows of table 2) have the same value of $\rho\beta\alpha = 4$ and different values of a^* such as 1.0, 1.5 and 2.0. The actual property ratio values of the silicone oil–water system have been listed in the fourth row of table 2. Figure 36 compares the neutral curves of the respective fluid combinations from tables 1 and 2, at $AR = 2.0$. Except for the small offset in the zones of oscillatory excitation and a proportional change in the Ra_{cr} values (as per the modified property ratios), the new neutral curves exactly corroborate the aforementioned findings of §§ 3.1–3.4. Precisely, figure 36 reveals that the ranges of interfacial heights corresponding to the onset of oscillatory convection are nearly equal, for all of the related fluid systems. The curves also reaffirm the narrowing of the oscillatory regime with the deviation of a^* value from unity. However, a small rightward bias is observed for the fluid systems of table 2. This can be construed to occur due to their large β value that renders the top layer to be more sensitive to thermal perturbation transferred across the interface. In addition, the lower α value also delays the dissipation of any imposed thermal fluctuations. Hence, the top layer is susceptible to undergo (thermal) fluctuation-induced flow reversals, even when the bottom layer has a slightly dominant convection. As a result, the regime of oscillatory convection (or the intersection point of neutral curves) for fluid systems listed in table 2 shifts to higher interfacial heights. Nevertheless, this behaviour can also be influenced by other factors/parameters whose characterisation requires some more meticulous analyses that are beyond the scope of the present work.
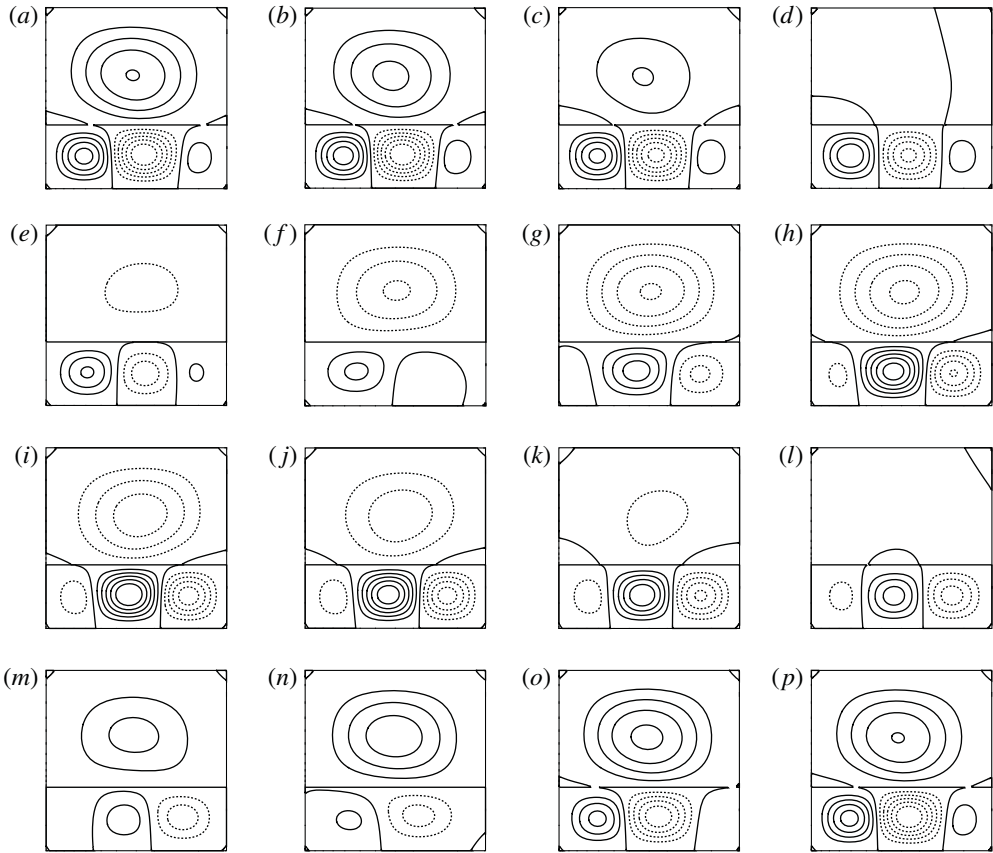
FIGURE 30. Streamlines of flow showing modulated TW mechanism at onset for $a^* = 0.50$, $AR = 1.0$ and $Y_f = 0.351$: (*a*) $t = 0$; (*b*) $t = T/15$; (*c*) $t = 2T/15$; (*d*) $t = T/5$; (*e*) $t = 4T/15$; (*f*) $t = T/3$; (*g*) $t = 2T/5$; (*h*) $t = 7T/15$; (*i*) $t = 8T/15$; (*j*) $t = 3T/5$; (*k*) $t = 2T/3$; (*l*) $t = 11T/15$; (*m*) $t = 4T/5$; (*n*) $t = 13T/15$; (*o*) $t = 14T/15$; (*p*) $t = T$.

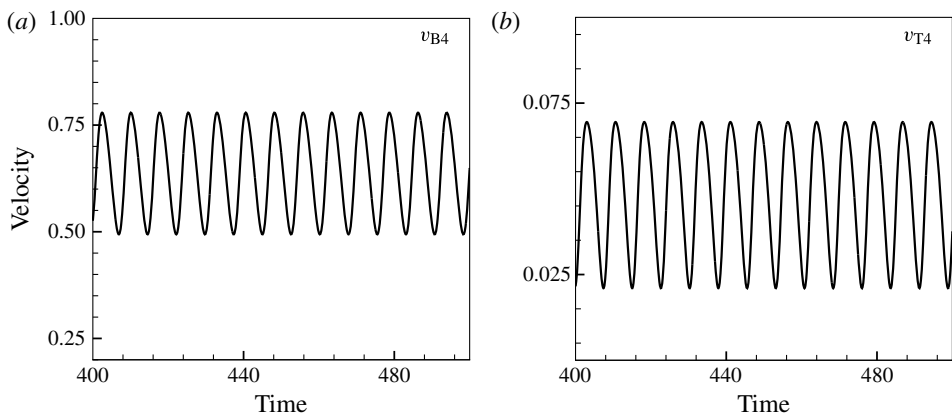FIGURE 31. Temporal variation of the v-velocity at various points on systems with $a^* = 0.50$: (*a*); B4 (*b*) T4.
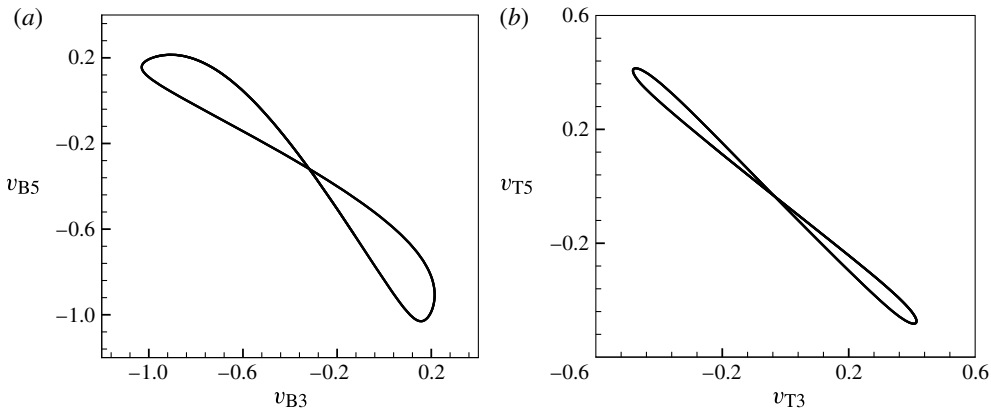
FIGURE 32. Phase variations in v-velocity of different points on the domain with $a^* = 0.50$; (*a*) B3 versus B5; (*b*) T3 versus T5.
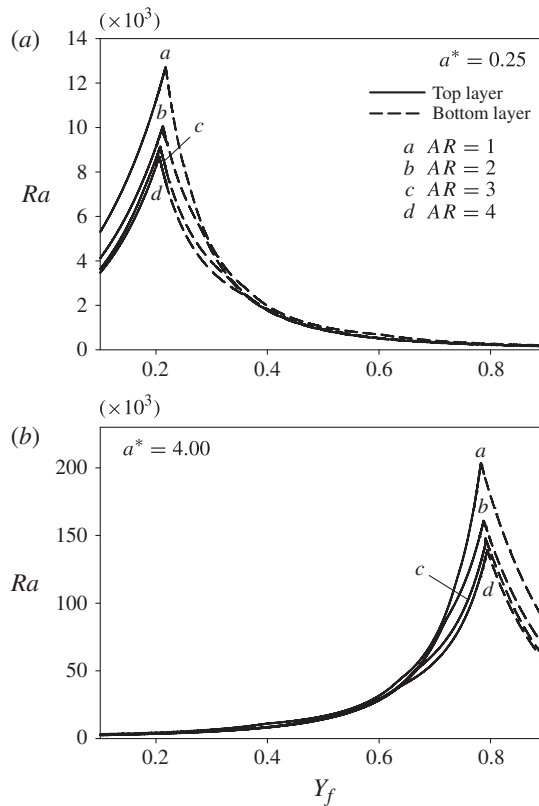

FIGURE 33. Neutral curves for the two-layer system with (*a*) $a^* = 0.25$; (*b*) $a^* = 4.00$.

Interestingly, the above facts also divulge the exact reason for the non-oscillatory behaviour exhibited by the silicone oil–water system when considered under the influence of pure buoyancy forces (Nepomnyashchy & Simanovskii 2004; Simanovskii & Nepomnyashchy 2006). The neutral curves for the onset of convection in silicone
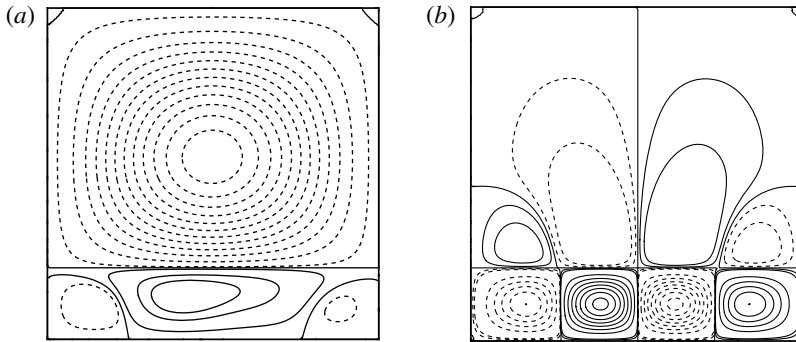
FIGURE 34. Streamlines at onset of flow in the two-layer system with $a^* = 0.25$ and $AR = 1.0$: (a) $Y_f = 0.216$; (b) $Y_f = 0.219$.
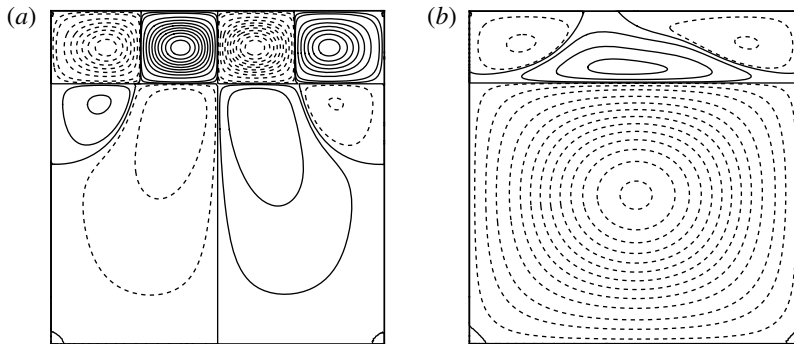

FIGURE 35. Streamlines at onset of the flow in the two-layer system with $a^* = 4.0$ and $AR = 1.0$: (a) $Y_f = 0.781$; (b) $Y_f = 0.784$.

S. no.	ρ	ν	κ	α	β	Pr	$\rho\beta\alpha$	a^*
1	0.8687	3.479	2.00	0.8135	5.66	25.7	4.00	1.00
2	0.8687	0.687	2.00	0.8135	5.66	25.7	4.00	1.50
3	0.8687	0.217	2.00	0.8135	5.66	25.7	4.00	2.00
4	0.8687	2.00	0.184	0.778	5.66	25.7	3.825	2.11
5	0.50	2.00	0.5	2.00	2.00	1.00	2.00	1.00
6	0.50	0.80	0.247	2.00	2.00	1.00	2.00	1.50
7	0.50	2.00	0.50	4.00	4.00	1.00	8.00	1.00
8	0.50	0.80	0.247	4.00	4.00	1.00	8.00	1.50

TABLE 2. Balanced contrast of the silicone oil–water system and balanced contrast of properties for varying $\rho\beta\alpha$.

oil–water system at different aspect ratios are shown in figure 37. Evidently, the system is devoid of any oscillatory regimes and the corresponding reason can be directly inferred from its values of $\rho\beta\alpha$ ($= 3.825$) and a^* ($= 2.11$). With these properties, the silicone oil–water system is closer to the fictitious $a^* = 2.00$ system considered in the current work. However, owing to its slightly higher a^* value, the disappearance of even the small patches of oscillatory regimes as observed for $a^* = 2.0$
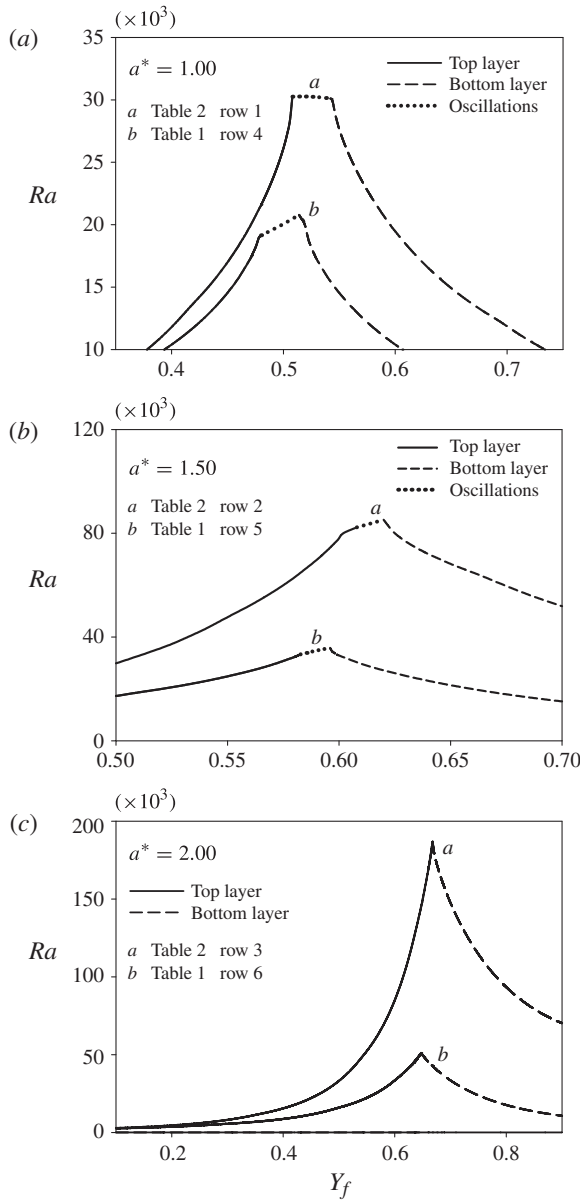
FIGURE 36. Neutral curves for the two layer system with $AR = 2.0$ and: (a) $a^* = 1.00$; (b) $a^* = 1.50$; (c) $a^* = 2.00$.

(at lower AR) is justified. This is further confirmed by the reduction in $\rho\beta\alpha$, based on which the range for oscillatory excitation (with respect to a^*) can be expected to shrink. To prove this point, fluid systems with different $\rho\beta\alpha$ combinations (2, 4 and 8) have been considered. Figure 38 shows their corresponding neutral curves at $AR = 2.0$ and $a^* = 1.0$, 1.5 where the expansion of the oscillatory regime with the increase in $\rho\beta\alpha$ is undoubtedly established.
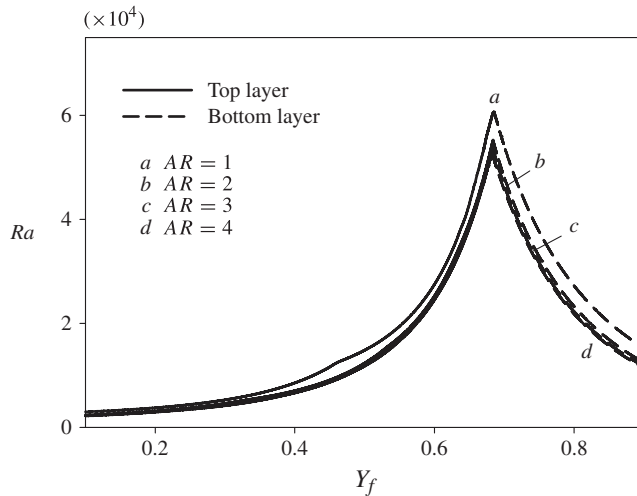
$(\times 10^4)$

FIGURE 37. Neutral curves for the two-layer silicone oil–water system.

The other important aspect of the current results which is worth re-emphasising is the occurrence of modulated TWs. While the range for the occurrence of oscillatory excitation is determined by the $\rho\beta\alpha$ and a^* values as discussed above, the criterion for the manifestation of modulated TWs (both periodic and quasi-periodic) additionally depends on the aspect ratio of the system. This primarily requires the critical height ratio a^* to be different from unity, so that the oscillatory excitation in the fluid layers occurs at unequal heights. Resultantly, at a particular aspect ratio of the system, the individual aspect ratios of the fluid layers will yield different fundamental modes (critical wavenumbers) of excitation in the layers. Owing to this disparate excitation (m:n resonance), a dynamic adjustment of convection rolls in the layers is necessitated and, thus, the system exhibits modulated TW phenomena. Correspondingly, for the present fluid systems with $a^* = 0.667$ and 1.50, the modulated TW was found to occur as l:$l+1$ resonance whereas for the systems with $a^* = 0.5$ and 2.0, it found to be associated with m:n resonance modes. It may be noted that these are very specific instances of resonance modes that have been obtained by selectively performing full nonlinear simulations. However, a complete bifurcation diagram representing all of the possible resonance modes can be obtained by a systematic weak nonlinear analysis. Also, the modes that have been obtained here mainly pertain to the two-dimensional situations. Owing to the third dimension, these modes will certainly be different for the 3D problem, as recently shown by Xie & Xia (2013).

4. Conclusions

From the neutral curves and flow patterns of various fluid combinations presented in this study, some important inferences can be obtained. Primary among them is the fact that flow onset characteristics for confined systems are largely dependent on the aspect ratio (*AR*) in addition to the height ratio (*a*) between the two fluids. At times, they are quite distinct from the characteristics of unconfined system comprising of same fluids and interfacial configuration (height). This can be ascertained from the tendencies shown by confined systems for oscillatory convection when the behaviour of the corresponding unconfined system is non-oscillatory and vice versa. In addition
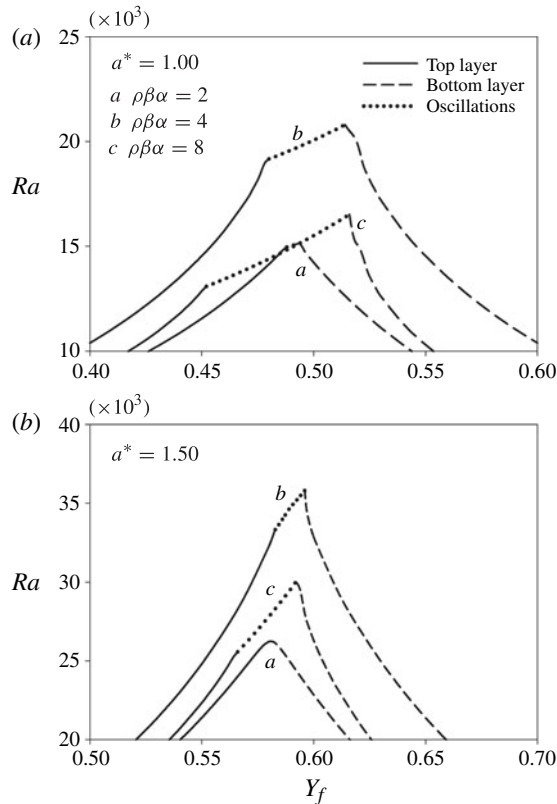
FIGURE 38. Neutral curves for the two-layer system with $AR = 2.0$ and: (*a*) $a^* = 1.00$; (*b*) $a^* = 1.50$.

to such distinctions, unique features are also exhibited in the oscillatory regimes wherein modulated TWs are observed at discrete aspect ratios for which the critical excitation wavenumber in the two layers are dissimilar (*m:n* resonance). In all the other situations involving similar critical wavenumbers, the oscillations are characterised by a SW pattern. It may be noted that the behaviour of oscillating unconfined systems primarily corresponds to that of a TW.

The other important conclusion that can be derived from the results is the ability of critical height ratio (a^*) to complement the property combination $\rho\beta\alpha$ in identifying the chances for oscillatory convection in any given system. It is now well established that the condition concerning $\rho\beta\alpha$ (either $\gg 1$ or $\ll 1$) alone cannot provide complete information on the possibility for onset of oscillatory flow. This can be corroborated from the absence of oscillatory onset for systems with $a^* = 0.25$ and $a^* = 4.00$ despite possessing a $\rho\beta\alpha$ value of 4. Yet, the criterion suggested by Renardy (1996) cannot be wholly omitted since it is associated with the non-self-adjointness of the corresponding matrices and, thus, forms a necessary condition for oscillations in the systems. Interestingly, the current work shows that a sufficient condition in this regard can be successfully identified with the additional consideration of a^* values. It is important to note here that the ranges of a^* ($0.5 < a^* < 2$) for which oscillatory

behaviour is observed in the current work are exclusive to the fluid combination with $\rho\beta\alpha = 4$. Correspondingly, it has been shown that the oscillatory range of a^* may either widen or become narrow based on the remoteness or closeness of $\rho\beta\alpha$ value to unity. This is consistent with the observations made for the silicone oil–water system which does not show any oscillatory modes when considered under the influence of pure buoyancy forces. However, with the consideration of thermocapillary effects, this fluid combination possesses onset of oscillatory convection as observed in the experiments of Degen *et al.* (1998).

Supplementary movies

Supplementary movies are available at http://dx.doi.org/10.1017/jfm.2014.359.

REFERENCES

BUSSE, F. H. 1981 On the aspect ratios of two-layer mantle convection. *Phys. Earth Planet. Inter.* **24** (4), 320–324.

CHORIN, A. J. 1968 Numerical solution of the Navier–Stokes equations. *Maths Comput.* **22** (104), 745–762.

COLINET, P. & LEGROS, J. C. 1994 On the Hopf bifurcation occurring in the two-layer Rayleigh–Bénard convective instability. *Phys. Fluids* **6**, 2631–2639.

COLINET, P., LEGROS, J. C. & VELARDE, M. G. 2001 *Nonlinear Dynamics of Surface-Tension-Driven Instabilities*. Wiley-VCH.

DEGEN, M. M., COLOVAS, P. W. & ANDERECK, C. D. 1998 Time-dependent patterns in the two-layer Rayleigh–Bénard system. *Phys. Rev.* E **57** (6), 6647–6659.

DENNIS, S. C. R. & QUARTAPELLE, L. 1983 Direct solution of the vorticity-stream function ordinary differential equations by a Chebyshev approximation. *J. Comput. Phys.* **52** (3), 448–463.

DIWAKAR, S. V., DAS, S. K. & SUNDARARAJAN, T. 2014 Accurate solutions of Rayleigh Bénard convection in confined two layer systems using spectral domain decomposition method. *Numer. Heat Transfer* A; 10.1080/10407782.2014.901048.

GOTTLIEB, D. & SHU, C. W. 1997 On the Gibbs phenomenon and its resolution. *SIAM Rev.* **39** (4), 644–668.

HEWITT, E. & HEWITT, R. E. 1979 The Gibbs–Wilbraham phenomenon: an episode in Fourier analysis. *Arch. Hist. Exact Sci.* **21** (2), 129–160.

JOHNSON, E. S. 1975 Liquid encapsulated floating zone melting of gaas. *J. Cryst. Growth* **30** (2), 249–256.

JOHNSON, D. & NARAYANAN, R. 1996 Experimental observation of dynamic mode switching in interfacial-tension-driven convection near a codimension-two point. *Phys. Rev.* E **54** (4), 3102–3104.

JOHNSON, D. & NARAYANAN, R. 1997 Geometric effects on convective coupling and interfacial structures in bilayer convection. *Phys. Rev.* E **56** (5), 5462–5472.

NATAF, H. C., MORENO, S. & CARDIN, P. 1988 What is responsible for thermal coupling in layered convection? *J. Phys.* **49** (10), 1707–1714.

NEPOMNYASHCHY, A. A. & SIMANOVSKII, I. B. 2004 Influence of thermocapillary effect and interfacial heat release on convective oscillations in a two-layer system. *Phys. Fluids* **16**, 1127–1139.

RASENAT, S., BUSSE, F. H. & REHBERG, I. 1989 A theoretical and experimental study of double-layer convection. *J. Fluid Mech.* **199**, 519–540.

RENARDY, Y. Y. 1996 Pattern formation for oscillatory bulk-mode competition in a two-layer Bénard problem. *Z. Angew. Math. Phys.* **47** (4), 567–590.

RENARDY, Y. Y., RENARDY, M. & FUJIMURA, K. 1999 Takens–Bogdanov bifurcation on the hexagonal lattice for double-layer convection. *Physica* D **129** (3), 171–202.

RICHTER, F. M. & JOHNSON, C. E. 1974 Stability of a chemically layered mantle. *J. Geophys. Res.* **79** (11), 1635–1639.

SABBAH, C. & PASQUETTI, R. 1998 A divergence-free multidomain spectral solver of the Navier–Stokes equations in geometries of high aspect ratio. *J. Comput. Phys.* **139** (2), 359–379.

SHEN, Y., NEITZEL, G. P., JANKOWSKI, D. F. & MITTELMANN, H. D. 1990 Energy stability of thermocapillary convection in a model of the float-zone crystal-growth process. *J. Fluid Mech.* **217** (1), 639–660.

SIMANOVSKII, I. B. & NEPOMNYASHCHY, A. A. 2006 Nonlinear development of oscillatory instability in a two-layer system under the combined action of buoyancy and thermocapillary effect. *J. Fluid Mech.* **555**, 177–202.

XIE, YI.-C. & XIA, KE.-Q. 2013 Dynamics and flow coupling in two-layer turbulent thermal convection. *J. Fluid Mech.* **728** (R1), 1–14.

ZEREN, R. W. & REYNOLDS, W. C. 1972 Thermal instabilities in two-fluid horizontal layers. *J. Fluid Mech.* **53** (2), 305–327.